

Influence of Nuclear Networks, Metallicity and Mixing on Stellar Evolution



Samuel Muthu
Lennard-Jones Laboratories, Astrophysics Group
Keele University

A Project Report submitted for the Summer Placement
August 2024

Abstract

This study, conducted as part of a summer placement on massive star models, provides a comprehensive analysis of nuclear reaction networks, initial metallicities, and convective boundary mixing and their influence on stellar evolution and the final fates of stars as supernovae, neutron stars, or black holes. Understanding these factors is critical for unraveling the life cycles and ultimate fates of stars. Specifically, these elements play a pivotal role in determining stellar luminosity, lifespan, and nucleosynthetic yields. Such characteristics not only affect the individual stars but also have broader implications for galactic chemical enrichment and the formation of subsequent generations of stars and planets.

The evolutionary models presented in this research were generated using the latest version (r24.03.1) of the MESA code. We examine the evolution of a $20 M_{\odot}$ star model across various nuclear networks, including `approx21_cr60_plus_co56.net`, `o_burn_full.net`, `mesa_128.net`, and `mesa_206.net`, to evaluate their differential effects on stellar evolution. In addition, we utilize the simplest nuclear network, `approx21_cr60_plus_co56.net`, alongside three distinct initial masses—15, 20, and $25 M_{\odot}$ —across a range of metallicities ($Z = Z_{\odot}$ to $Z = 10^{-7}$ and $Z = 0$). This multifaceted approach aids in understanding how mass and metallicity interactively influence stellar evolution.

Furthermore, we investigate the mechanisms of energy transport within stars by examining convective boundary mixing (CBM). By applying varying rates of CBM to our stellar models, we gain valuable insights into its significant role in shaping stellar structures and evolutionary pathways. The findings of this study enhance our understanding of the complexities involved in stellar evolution and contribute to the broader knowledge of astrophysical processes.

Acknowledgments

I would like to extend my heartfelt gratitude to my supervisor and professor, Dr. Raphael Hirschi, for his invaluable mentorship, guidance, and encouragement throughout this project. His profound expertise in stellar evolution and nuclear astrophysics has greatly enriched my understanding, and his unwavering support has been a constant source of motivation. I am deeply inspired by his dedication to the field and am motivated to continue learning under his supervision as I pursue my Independent Study Project on ‘Modelling first stars with zero metallicity’ in my third year.

I am also immensely grateful to Vishnu and Em, members of the Stellar Hydrodynamics, Nucleosynthesis, and Evolution Group, for their generous assistance and insightful discussions. Their collaborative spirit and technical knowledge in stellar hydrodynamics and nucleosynthesis have provided me with essential perspectives, helping me overcome challenges and deepen my comprehension of the complex models used in this study. I truly appreciate their willingness to share their expertise and offer guidance whenever needed.

Contents

Abstract	ii
Acknowledgments	iii
List of Figures	vii
List of Tables	viii
1 Introduction	1
2 Stellar Structure and Evolution	1
2.1 Differential Equations of Stellar Evolution	1
2.2 Model Properties	2
2.2.1 Convection - Schwarzschild criterion	2
2.2.2 Mass loss and Rotation	3
2.3 Methods for Investigating Stellar Evolution	3
2.3.1 Kippenhahn Diagram	3
2.3.2 Hertzsprung-Russell Diagram (HRD)	3
3 Model Parameters	5
3.1 Nuclear Reaction Networks	5
4 Numerical Results	8
4.1 Nuclear Networks	8
4.2 Metallicity and Mass	12
4.3 Convective Boundary Mixing	12
5 Pre-Supernova Abundance	21
5.1 ^{12}C Yields and Mass Fractions	21
5.2 ^{14}N Yields and Mass Fractions	24
5.3 ^{16}O Yields and Mass Fractions	27
6 Analysis of Burning Stages	31
6.1 Across Nuclear Networks	31
6.1.1 Main Sequence and Hydrogen Burning	31
6.1.2 Transition to Helium Burning	31
6.1.3 Carbon Ignition and Late Burning Stages	32
6.1.4 Impact on Final Evolutionary Pathways	32
6.2 Across Metallicity and Mass	32
6.2.1 Hydrogen and Helium Burning: Foundations for Later Evolution . . .	33
6.2.2 Carbon Burning: Influence of Metallicity and Mass	34
6.2.3 Oxygen Burning: The Final Hydrostatic Stage	34
6.2.4 Final Remnant Formation and Supernovae	35
6.3 Across various rates of CBM	35

6.3.1	CBM and Hydrogen Burning: Core Growth and Main Sequence Evolution	35
6.3.2	CBM and Helium Burning: Effects on Core Structure and Mixing	36
6.3.3	CBM and Advanced Burning: Implications for Carbon and Oxygen Burning	37
6.3.4	Implications for Supernova Progenitors and Final Remnants	37
7	Pre-Supernova Abundance Analysis of Fundamental Elements	38
7.1	General Trends in ^{12}C	38
7.1.1	Impact of Convective Boundary Mixing (CBM)	38
7.1.2	Radial Distribution of ^{12}C Mass Fraction	39
7.1.3	Comparative Plots of $M_{12}\text{C}$ vs. $\log(Z)$	39
7.1.4	Summary of Key Observations	40
7.2	General Trends in ^{14}N Yields	42
7.2.1	Metallicity Dependence	42
7.2.2	Effect of Stellar Mass:	42
7.2.3	Influence of CBM Rates:	42
7.2.4	Radial Distribution of ^{14}N Mass Fraction	43
7.2.5	Summary of Key Observations	43
7.3	General Trends in ^{16}O Yields	46
7.3.1	Metallicity Dependence	46
7.3.2	Impact of Stellar Mass	46
7.3.3	Effect of CBM Rates	46
7.3.4	Radial Distribution of ^{16}O Mass Fraction	47
7.3.5	Summary of Key Observations	47
8	Conclusion	50
9	References	50

List of Figures

1	Kippenhahn Diagram illustrating the evolution of the star's internal structure, with convective and radiative zones indicated by a color gradient over time.	4
2	Evolution of the models in the HRD, showing the transition from the Zero Age Main Sequence (ZAMS) through core hydrogen exhaustion and subsequent evolution.	4
3	Evolution of the $20M_{\odot}$ model core in temperature (T_c) and density (ρ_c) plane.	8
4	A detailed look in the $T_c - \rho_c$ plane during advance burning stages	8
5	HR Diagram for the $20M_{\odot}$ models with different nuclear networks; the coloured dots on the path respectively refer to main sequence phase / H ignition (Pink), core H exhaustion / He ignition (Green), core He exhaustion / C ignition (Red).	8
6	Evolution of Ye vs Tc for different nuclear networks	9
7	Kippenhahn plots for the $20M_{\odot}$ models with different nuclear networks.	10
9	Core and Surface evolution for the $15M_{\odot}$ models with various metallicities.	17
10	Core and Surface evolution for the $20M_{\odot}$ models with various metallicities.	17
11	Core and Surface evolution for the $25M_{\odot}$ models with various metallicities.	17
12	Core and surface evolution for the $15M_{\odot}$ models at different CBM factors.	18
13	Core and surface evolution for the $20M_{\odot}$ models at different CBM factors.	19
14	Core and surface evolution for the $25M_{\odot}$ models at different CBM factors.	20
15	Comparison of ^{12}C Mass Yield (left) and Mass Fraction (right) for a $15M_{\odot}$ model at various metallicities, categorised by CBM Rates.	22
16	Comparison of ^{12}C Mass Yield (left) and Mass Fraction (right) for a $20M_{\odot}$ model at various metallicities, categorised by CBM Rates.	23
17	Comparison of ^{12}C Mass Yield (left) and Mass Fraction (right) for a $25M_{\odot}$ model at various metallicities, categorised by CBM Rates.	24
18	Comparison of ^{14}N Mass Yield (left) and Mass Fraction (right) for a $15M_{\odot}$ model at various metallicities, categorised by CBM Rates.	25
19	Comparison of ^{14}N Mass Yield (left) and Mass Fraction (right) for a $20M_{\odot}$ model at various metallicities, categorised by CBM Rates.	26
20	Comparison of ^{14}N Mass Yield (left) and Mass Fraction (right) for a $25M_{\odot}$ model at various metallicities, categorised by CBM Rates.	27
21	Comparison of ^{16}O Mass Yield (left) and Mass Fraction (right) for a $15M_{\odot}$ model at various metallicities, categorised by CBM Rates.	28
22	Comparison of ^{16}O Mass Yield (left) and Mass Fraction (right) for a $15M_{\odot}$ model at various metallicities, categorised by CBM Rates.	29
23	Comparison of ^{16}O Mass Yield (left) and Mass Fraction (right) for a $15M_{\odot}$ model at various metallicities, categorised by CBM Rates.	30
24	^{12}C Mass Yield Comparisons for $15, 20$ and $25M_{\odot}$ star respectively.	41
25	^{14}N Mass Yield Comparisons for $15, 20$ and $25M_{\odot}$ star respectively.	45
26	^{16}O Mass Yield Comparisons for $15, 20$ and $25M_{\odot}$ star respectively.	49

List of Tables

1	List of isotopes employed in the <code>approx21_cr60_plus_co56.net</code> nuclear network; elements ^{60}Cr and ^{56}Co were included in the network.	5
2	List of isotopes employed in the <code>o_burn_full.net</code> nuclear network	6
3	List of isotopes employed in the <code>mesa_128.net</code> nuclear network	6
4	List of isotopes employed in the <code>mesa_206.net</code> nuclear network	7
5	Physical properties of evolutionary models with different nuclear networks .	11
6	Properties of models with varying mass and metallicity during H burning stage	13
7	Properties of models with varying mass and metallicity during He burning stage.	14
8	Properties of models with varying mass and metallicity during C burning stage.	15
9	Properties of models with varying mass and metallicity during O burning stage.	16

1 Introduction

Gravitational compression in the core of stars fuse lighter elements into heavier ones, which persist until the energy generated from the nuclear reactions is able to withhold it's own gravity. Simpler nuclear processes, such as hydrogen and helium burning, are well understood with straightforward reactions. However, as a star evolves into later stages—like carbon, neon, oxygen, and silicon burning—nuclear processes become increasingly complex. Detailed networks are essential to model these stages, capturing the diverse reactions that govern elemental synthesis and distribution. During the burning stages, the stellar plasma is continually mixed between its convective and radiative zones, a process known as Convective Boundary Mixing (CBM). This influences nuclear reaction rates, making it vital for understanding stellar evolution. Although nuclear networks and CBM define what occurs in the core of a star, their initial conditions have a huge impact on them like mass and metallicity. For instance, massive stars, with higher core temperatures, undergo rapid and intense nuclear burning, leading to shorter lifetimes and explosive end stages like supernovae. In contrast, lower-mass stars burn fuel more slowly, resulting in longer lifetimes and gentler outcomes, such as white dwarfs. Hence models with various masses and metallicities are included in the study.

2 Stellar Structure and Evolution

To analyze the influence of factors like initial mass, metallicity, CBM, and nuclear networks on stellar evolution, uniform and comprehensive stellar models are essential. This paper uses the latest MESA code (r24.03.01), with Section 2.1 covering the governing equations, Section 2.2 detailing model properties, and Section 2.3 explaining tools used to study stellar evolution.

2.1 Differential Equations of Stellar Evolution

The fundamental equations that govern stellar evolution are as follows:

Conservation of Mass

$$\frac{\partial r}{\partial m} = \frac{1}{4\pi r^2 \rho} \quad (2.1)$$

Dynamic Equation of Pressure

$$\frac{\partial P}{\partial m} = -\frac{Gm}{4\pi r^4} - \frac{1}{4\pi r^4} \frac{\partial^2 r}{\partial t^2} \quad (2.2)$$

Conservation of Energy

$$\frac{\partial l}{\partial m} = \epsilon_{\text{nuc}} - \epsilon_\nu - T \frac{\partial s}{\partial t} \quad (2.3)$$

l : luminosity at a given mass shell, s : entropy, ϵ_ν : energy lost due to neutrino emission, ϵ_{nuc} : energy generation rate per unit mass due to nuclear reactions.

Temperature Gradient Equation

$$\frac{\partial T}{\partial m} = -\frac{Gm}{4\pi r^4} \frac{T}{P} \nabla, \quad \text{with} \quad \nabla = \begin{cases} 3\kappa \nabla_{\text{rad}} = \frac{lP}{mT^4} & \text{if } \nabla_{\text{rad}} \leq \nabla_{\text{ad}} \\ \nabla_{\text{ad}} + \Delta\nabla & \text{if } \nabla_{\text{rad}} > \nabla_{\text{ad}} \end{cases} \quad (2.4)$$

∇ : Temperature gradient, $\Delta\nabla$: Convective adjustment: the difference between the actual temperature gradient and the adiabatic temperature gradient.

Abundance Evolution

$$\frac{\partial X_i}{\partial t} = \frac{A_i m_u}{\rho} \left(-\sum_j (1 + \delta_{ij}) r_{ij} + \sum_{k,l} r_{kl,i} \right) \quad [\text{+ mixing terms}] \quad i = 1 \dots N \quad (2.5)$$

X_i : Abundance of species i (e.g., hydrogen, helium), A_i : Atomic mass of species i , \mathbf{m}_u : Atomic mass unit, r_{ij} : Reaction rates for the transformation of species j to i , δ_{ij} : Kronecker delta, which is 1 if $i = j$ and 0 otherwise.

N.B: Equation 1.2 is written in its general form, without assuming hydrostatic equilibrium, if we assume the star to be in hydrostatic equilibrium the equation is written as follows:

$$\frac{\partial P}{\partial m} = -\frac{Gm}{4\pi r^4} \quad (2.6)$$

The term $\Delta\nabla$ in equation 1.4, represents the superadiabaticity of the temperature gradient, which arises from a theory of convection (typically, the mixing length theory). In the star's interior, $\Delta\nabla$ can be considered zero, except in the outermost layers.

2.2 Model Properties

2.2.1 Convection - Schwarzschild criterion

$$\nabla_{\text{rad}} > \nabla_{\text{ad}} \quad (2.7)$$

Schwarzschild criterion is used to determine the convective zones with overshoot parameters set at 0.5, 0.2 and 0.05. According to the Schwarzschild criterion, we can expect convection to occur if

$$\nabla_{\text{rad}} = \frac{3P}{16\pi acG} \frac{T^4}{\kappa l} > \nabla_{\text{ad}}$$

Where κ represents opacity, l represents the luminosity, and a represents the radiation constant, $a = 7.5657 \times 10^{-16} \text{ J m}^{-3} \text{ K}^{-4}$.

2.2.2 Mass loss and Rotation

Mass loss and Rotation were not applied to the stellar models.

2.3 Methods for Investigating Stellar Evolution

2.3.1 Kippenhahn Diagram

The Kippenhahn Diagram is an invaluable tool for probing the internal structure of stars and understanding their evolutionary processes. In this diagram, the stellar age is plotted against the radial mass coordinate, effectively mapping the star's internal layers over time. The diagram uses a color gradient to distinguish between convective and radiative zones, thus illustrating how energy is generated and transported within the star. Early in a star's life, for example, a prominent convective core is often visible, indicating regions where vigorous mixing and energy transport occur. As the star evolves, shifts in these zones reflect changes in nuclear burning and energy transport mechanisms.

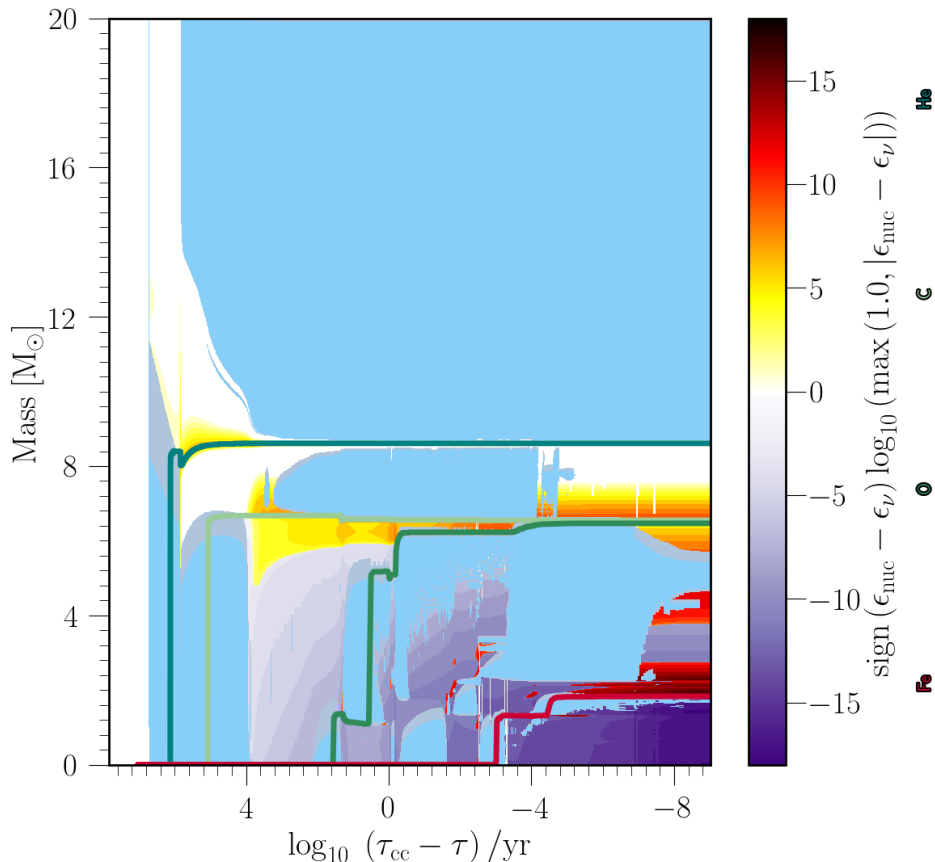


Figure 1: Kippenhahn Diagram illustrating the evolution of the star's internal structure, with convective and radiative zones indicated by a color gradient over time.

2.3.2 Hertzsprung-Russell Diagram (HRD)

The Hertzsprung-Russell Diagram (HRD) is a fundamental diagnostic tool in astrophysics that plots a star's luminosity against its surface temperature (or spectral class). This diagram provides a snapshot of a star's evolutionary trajectory over time. Stars begin their lives on the Zero Age Main Sequence (ZAMS), where they steadily fuse hydrogen in their cores. As a star evolves, structural changes—such as the depletion of core hydrogen—cause its position on the HRD to shift dramatically. For instance, a steep increase in luminosity is typically observed as the star exhausts its hydrogen fuel; the contracting core heats up

rapidly, resulting in a sharp rightward turn on the HRD. This characteristic change marks the transition from main-sequence evolution to later stages.

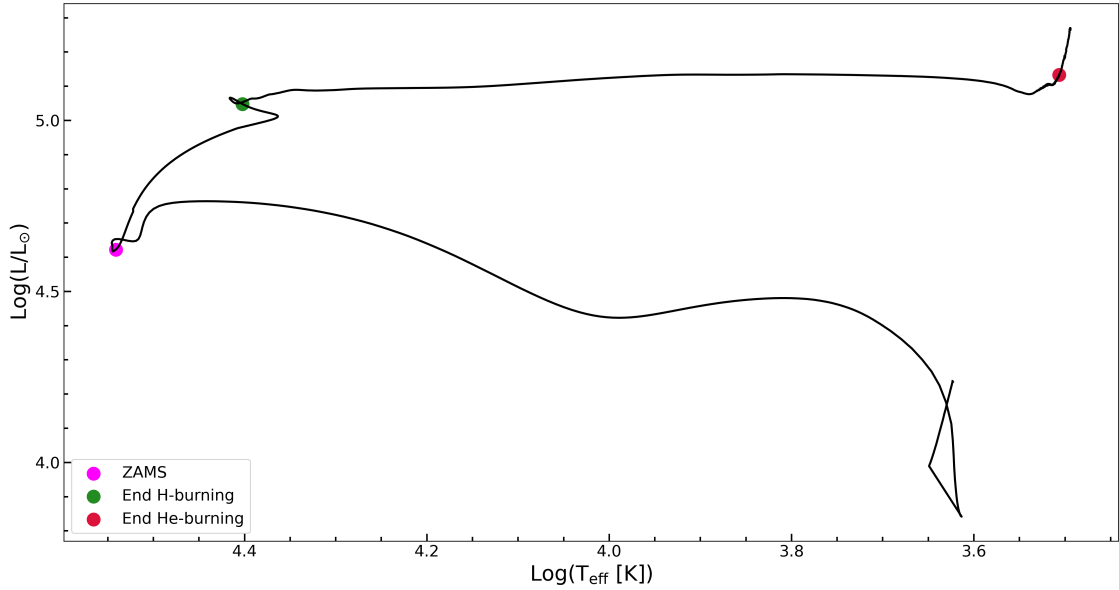


Figure 2: Evolution of the models in the HRD, showing the transition from the Zero Age Main Sequence (ZAMS) through core hydrogen exhaustion and subsequent evolution.

3 Model Parameters

3.1 Nuclear Reaction Networks

The nuclear networks used in models differ primarily in the complexity and scope of reactions they calculate, not just in the number of isotopes they include. Networks with more isotopes enable a greater variety of reactions, increasing the model's accuracy in simulating stellar burning stages. Simpler networks, like the basic or default network `approx21_cr60_plus_co56.net` (A21), focus on essential isotopes and reactions needed to model primary stages of nuclear burning.

Element	Z	A _{min}	A _{max}	Element	Z	A _{min}	A _{max}	Element	Z	A _{min}	A _{max}
n	0	1		Ne	10	20		Cr	24	48	
p	1	1		Mg	12	24		Fe	26	52	
H	1	1		Si	14	38		Fe	26	54	
He	2	3	4	S	16	32		Fe	26	56	
C	6	12		Ar	18	36		Ni	28	56	
N	7	14		Ca	20	40		*Cr	24	60	
O	8	16		Ti	22	44		*Co	27	56	

Table 1: List of isotopes employed in the `approx21_cr60_plus_co56.net` nuclear network; elements ⁶⁰Cr and ⁵⁶Co were included in the network.

More comprehensive networks include additional isotopes, allowing for detailed modeling of advanced burning stages, which is crucial in accurately simulating late stellar evolution, in addition to A21, nuclear networks such as `o_burn_full.net`(OB), `mesa_128.net`(M128), and `mesa_206.net`(M206) were used in the study.

Element	Z	A_{min}	A_{max}	Element	Z	A_{min}	A_{max}	Element	Z	A_{min}	A_{max}
n	0	1	1	N	7	13	16	P	15	30	34
H	1	1	2	O	8	14	19	S	16	31	37
He	2	3	4	F	9	17	20	Cl	17	35	38
Li	3	6	7	Ne	10	18	23	Ar	18	35	41
Be	4	7		Na	11	21	24	K	19	39	44
Be	4	9	10	Mg	12	23	27	Ca	20	39	44
B	5	8		Al	13	25	28	Ca	20	46	
B	5	10	11	Si	14	27	33	Ca	20	48	
C	6	12	14								

Table 2: List of isotopes employed in the `o_burn_full.net` nuclear network

Element	Z	A_{min}	A_{max}	Element	Z	A_{min}	A_{max}	Element	Z	A_{min}	A_{max}
n	0	1	1	Ne	10	18	22	Sc	21	43	46
H	1	1	2	Na	11	21	24	Ti	22	44	48
He	2	3	4	Mg	12	23	26	V	23	47	51
Li	3	7		Al	13	25	28	Cr	24	48	57
Be	4	7		Si	14	27	30	Mn	25	51	56
Be	4	9	10	P	15	30	32	Fe	26	52	58
B	5	8		S	16	31	34	Co	27	55	60
C	6	12	13	Cl	17	35	37	Ni	28	55	61
N	7	14	15	Ar	18	35	38	Cu	29	59	62
O	8	14	18	K	19	39	43	Zn	30	60	64
F	9	17	19	Ca	20	39	44				

Table 3: List of isotopes employed in the `mesa_128.net` nuclear network

Element	Z	A_{min}	A_{max}	Element	Z	A_{min}	A_{max}	Element	Z	A_{min}	A_{max}
n	0	1	1	F	9	17	20	Ca	20	39	49
H	1	1	2	Ne	10	18	23	Sc	21	43	51
He	2	3	4	Na	11	21	24	Ti	22	43	54
Li	3	6	7	Mg	12	23	27	V	23	47	56
Be	4	7		Al	13	25	28	Cr	24	47	58
Be	4	9	10	Si	14	27	33	Mn	25	51	59
B	5	8		P	15	30	34	Fe	26	51	66
B	5	10	11	S	16	31	37	Co	27	55	67
C	6	12	13	Cl	17	35	38	Ni	28	55	68
N	7	13	16	Ar	18	35	41	Cu	29	59	66
O	8	14	19	K	19	39	44	Zn	30	59	66

Table 4: List of isotopes employed in the `mesa_206.net` nuclear network

4 Numerical Results

4.1 Nuclear Networks

This section presents the evolutionary sequences of a $20M_{\odot}$ model with four different nuclear networks with initial composition $Y = 0.26601$ (Ekström et al. 2012) and $Z = Z_{\odot} (\approx 0.014)$.

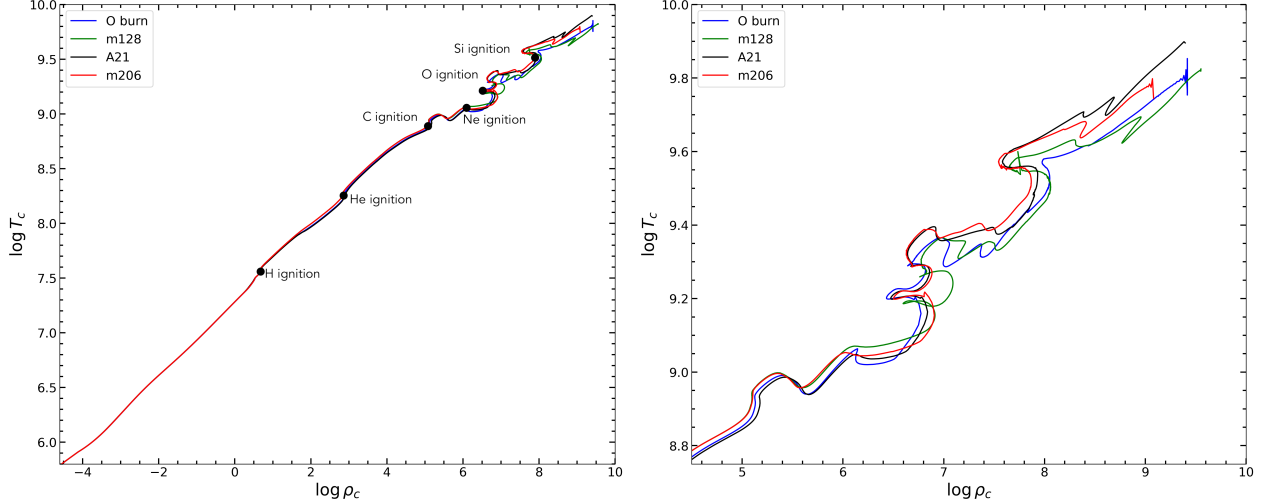


Figure 3: Evolution of the $20M_{\odot}$ model core in temperature (T_c) and density (ρ_c) plane during advance burning stages

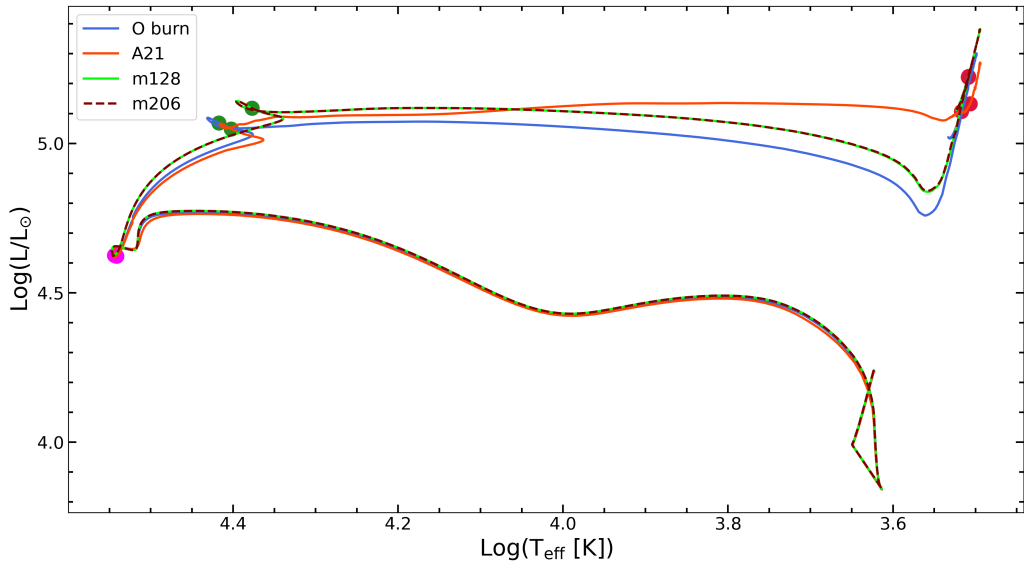


Figure 5: HR Diagram for the $20M_{\odot}$ models with different nuclear networks; the coloured dots on the path respectively refer to main sequence phase / H ignition (Pink), core H exhaustion / He ignition (Green), core He exhaustion / C ignition (Red).

Figure 5 shows the evolutionary change of the star's core properties, and Figure 7 illustrates the evolutionary tracks of the model in the HRD. Figures 6 and 7 depicts the evolution of Y_e against T_c and the Kippenhahn plots for the different nuclear networks, representing the evolution of the convective regions and the location of the burning shells in mass in the star's interior. Each of these burning shells is discussed in brief in latter sections.

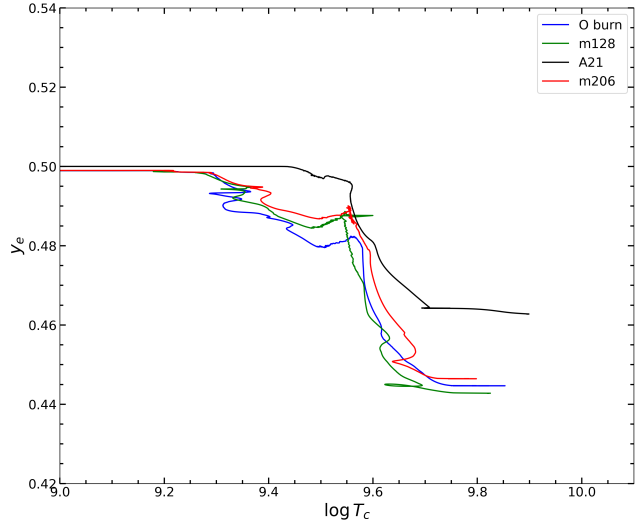


Figure 6: Evolution of Y_e vs T_c for different nuclear networks

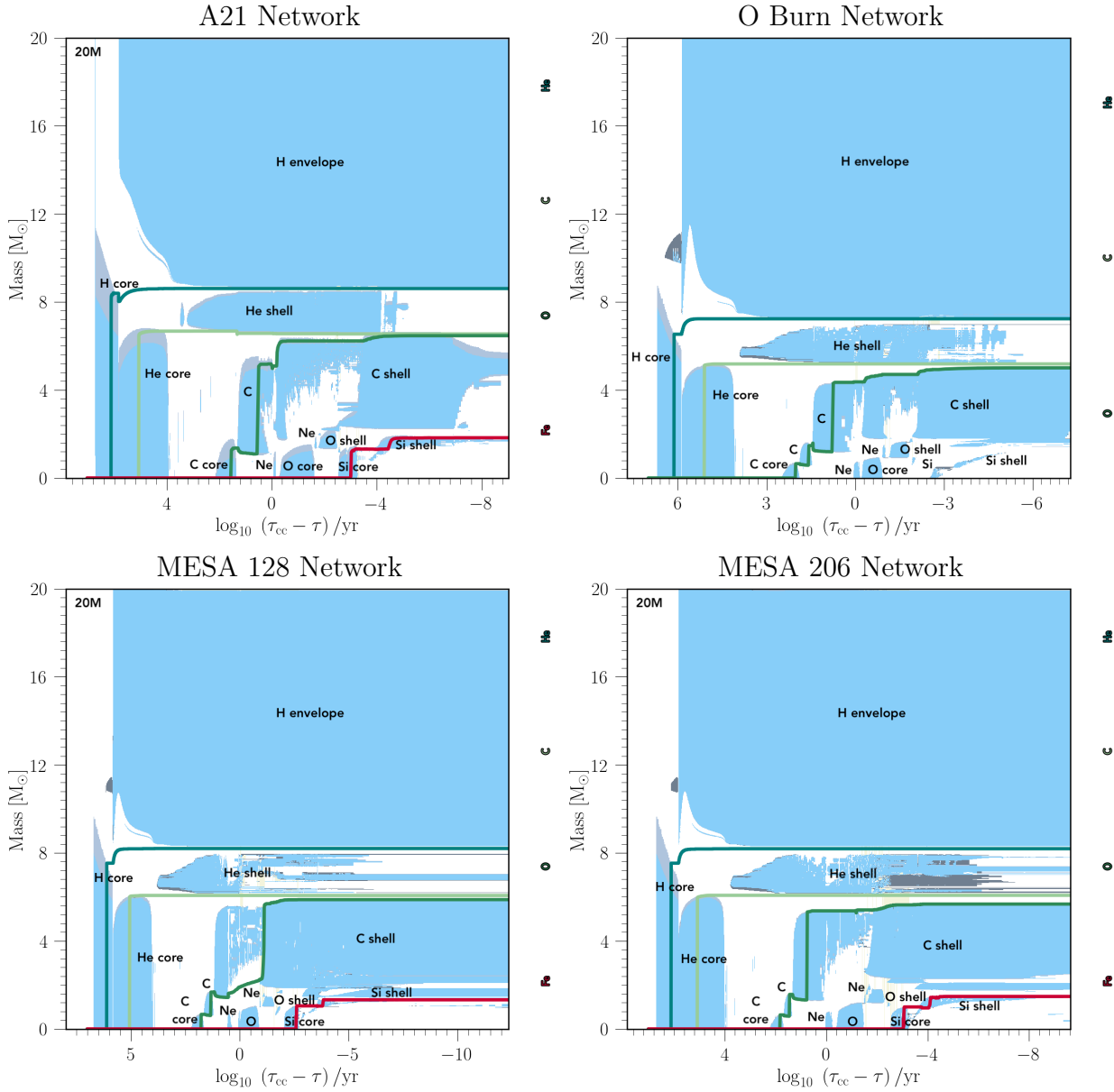


Figure 7: Kippenhahn plots for the $20M_\odot$ models with different nuclear networks.

Table 5: Physical properties of evolutionary models with different nuclear networks

Stage	Star Age (yr)	$\log L/L_\odot$	$\log T_{\text{eff}}$ (K)	T_c^a (10^7 K)	ρ_c^b (g/cm 3)	M_α^c (M_\odot)	$M_{C/O}^d$ (M_\odot)	$M_{O/Ne}^e$ (M_\odot)
20M$_\odot$, f=0.05, A21.net								
H_{ignition}	8.356×10^4	4.618	4.544	3.633	5.078	0.000	0.000	0.000
H_{exhaustion}	9.214×10^6	5.032	4.387	5.663	15.34	6.422	0.000	0.000
He_{ignition}	9.239×10^6	5.120	4.023	16.82	700.8	6.003	0.000	0.000
He_{exhaustion}	1.004×10^7	5.127	3.507	30.48	2948	6.897	4.865	0.000
C_{ignition}	1.006×10^7	5.240	3.496	60.16	3.892×10^4	6.907	4.865	0.000
C_{exhaustion}	1.006×10^7	5.270	3.494	108.2	1.085×10^6	6.907	4.866	1.446
O_{ignition}	1.006×10^7	5.264	3.494	166.1	5.018×10^6	6.906	4.866	4.224
O_{exhaustion}	1.006×10^7	5.265	3.495	238.3	1.779×10^7	6.906	4.865	4.358
20M$_\odot$, f=0.05, OB.net								
H_{ignition}	8.562×10^4	4.618	4.544	3.633	5.080	0.000	0.000	0.000
H_{exhaustion}	9.158×10^6	5.052	4.402	5.684	15.13	6.533	0.000	0.000
He_{ignition}	9.180×10^6	4.848	3.590	17.17	726.2	6.628	0.000	0.000
He_{exhaustion}	9.896×10^6	5.094	3.518	30.19	2738	7.234	5.184	0.000
C_{ignition}	9.910×10^6	5.301	3.499	82.69	1.353×10^5	7.235	5.185	0.000
C_{exhaustion}	9.911×10^6	5.298	3.499	110.0	1.077×10^6	7.235	5.185	1.533
O_{ignition}	9.911×10^6	5.293	3.499	168.3	4.273×10^6	7.235	5.185	4.368
O_{exhaustion}	9.911×10^6	5.294	3.499	231.2	3.753×10^7	7.235	5.185	4.706
20M$_\odot$, f=0.05, M128.net								
H_{ignition}	8.707×10^4	4.623	4.545	3.639	5.075	0.000	0.000	0.000
H_{exhaustion}	9.456×10^6	5.101	4.361	5.712	14.71	7.532	0.000	0.000
He_{ignition}	9.477×10^6	5.230	3.507	17.40	638.0	7.555	0.000	0.000
He_{exhaustion}	1.012×10^7	5.207	3.510	30.60	2525	8.194	6.067	0.000
C_{ignition}	1.014×10^7	5.382	3.494	86.07	1.252×10^5	8.200	6.068	0.000
C_{exhaustion}	1.014×10^7	5.379	3.494	111.8	9.390×10^5	8.200	6.068	1.685
O_{ignition}	1.014×10^7	5.376	3.494	154.0	9.668×10^6	8.200	6.068	1.785
O_{exhaustion}	1.014×10^7	5.378	3.495	226.1	2.727×10^7	8.200	6.066	2.612
20M$_\odot$, f=0.05, M206.net								
H_{ignition}	8.707×10^4	4.623	4.545	3.639	5.075	0.000	0.000	0.000
H_{exhaustion}	9.456×10^6	5.101	4.361	5.712	14.71	7.532	0.000	0.000
He_{ignition}	9.477×10^6	5.230	3.507	17.40	638.0	7.555	0.000	0.000
He_{exhaustion}	1.012×10^7	5.207	3.510	30.60	2525	8.194	6.067	0.000
C_{ignition}	1.014×10^7	5.381	3.495	87.00	1.275×10^5	8.190	6.073	0.000
C_{exhaustion}	1.014×10^7	5.379	3.494	111.8	9.390×10^5	8.200	6.068	1.685
O_{ignition}	1.014×10^7	5.376	3.494	154.0	9.668×10^6	8.200	6.068	1.785
O_{exhaustion}	1.014×10^7	5.378	3.495	226.1	2.727×10^7	8.200	6.066	2.612

Note: Superscripts a, b, c, d, e represent core temperature, core density, He, C/O and O/Ne core masses respectively.

4.2 Metallicity and Mass

This section showcases the evolution of massive stars models with three distinct initial masses: 15, 20, and $25 M_{\odot}$. These models are computed at seven different metallicities: solar metallicity, Z_{\odot} (≈ 0.0142), as well as lower metallicities of 10^{-3} , 10^{-4} , 10^{-5} , 10^{-6} , 10^{-7} , and finally a zero-metallicity case representative of Population III stars. This broad metallicity range enables us to assess the influence of chemical composition on stellar structure and evolution—from metal-rich environments to nearly primordial conditions.

The physical properties of these 21 models—each corresponding to a specific mass and metallicity combination at key burning stages—are summarized in Tables 6, 7, 8, and 9. Furthermore, Figures 9, 10, and 11 display the evolution of these models in both the HRD and the T_c - ρ_c plane, they illustrate how variations in mass and metallicity shape the evolutionary trajectories of stars, highlighting systematic trends such as shifts in luminosity and effective temperature during key phases of stellar evolution.

4.3 Convective Boundary Mixing

This section examines the impact of CBM on the evolution of massive stars by comparing models computed with three different overshoot parameters—corresponding to CBM rates of 5%, 2%, and 0.5%—for stars with initial masses of 15, 20, and $25 M_{\odot}$. CBM describes the process by which turbulent motions in convective zones penetrate into the adjacent radiative regions, thereby facilitating additional mixing beyond the classical convective boundaries defined by the Schwarzschild (or Ledoux) criteria.

By allowing convective eddies to overshoot into the stable layers, CBM can effectively enlarge the convective core, alter the chemical gradients, and extend the duration of core burning phases. These effects have significant consequences for the star’s evolutionary trajectory, influencing both the position of the star in the HRD and the T_c - ρ_c structure.

Figures 12, 13, and 14 illustrate the evolutionary tracks in both the HRD and the T_c - ρ_c plane for the 15, 20, and $25 M_{\odot}$ models with three different CBM rates respectively. These figures vividly demonstrate that higher CBM rates lead to more extended convective cores, longer main-sequence lifetimes, and systematic shifts in the evolutionary paths, while lower CBM rates result in more compact cores and alternate evolutionary characteristics.

Table 6: Properties of models with varying mass and metallicity during H burning stage

Z	M(M_{\odot})	Star Age (yr)	$\log(L/L_{\odot})$	$\log T_{\text{eff}}$ (K)	T_c^a (10^7 K)	ρ_c^b (g cm $^{-3}$)	M_{cc}^e (M_{\odot})
ZAMS (Hydrogen ignition)							
Z $_{\odot}$	15	1.524×10^5	4.270	4.492	3.463	6.554	5.758
	20	9.167×10^4	4.618	4.544	3.633	5.078	8.887
	25	6.528×10^4	4.869	4.580	3.758	4.241	12.44
10^{-3}	15	1.441×10^5	4.316	4.551	3.928	9.697	6.187
	20	8.719×10^4	4.650	4.597	4.117	7.492	9.419
	25	6.604×10^4	4.893	4.630	4.258	6.254	13.04
10^{-4}	15	1.419×10^5	4.325	4.584	4.403	13.68	6.255
	20	8.619×10^4	4.657	4.629	4.626	10.65	9.457
	25	6.778×10^4	4.899	4.662	4.792	8.928	13.07
10^{-5}	15	1.496×10^5	4.330	4.616	5.051	20.70	6.246
	20	9.190×10^4	4.661	4.662	5.320	16.23	9.445
	25	6.951×10^4	4.903	4.694	5.520	13.67	13.04
10^{-6}	15	1.476×10^5	4.335	4.649	5.824	31.80	6.213
	20	9.513×10^4	4.666	4.695	6.153	25.15	9.422
	25	7.345×10^4	4.907	4.728	6.397	21.30	13.01
10^{-7}	15	1.499×10^5	4.340	4.682	6.742	49.44	6.165
	20	9.573×10^4	4.671	4.729	7.152	39.57	9.357
	25	7.438×10^4	4.912	4.762	7.455	33.77	12.93
0	15	1.001×10^5	4.458	4.757	9.033	137.7	0.000
	20	7.807×10^4	4.780	4.828	10.85	151.6	1.325
	25	7.643×10^4	4.949	4.863	11.60	128.4	12.03
Hydrogen Exhaustion							
Z $_{\odot}$	15	1.581×10^7	4.913	4.283	5.571	17.01	4.452
	20	1.005×10^7	5.149	4.304	5.753	14.42	6.364
	25	7.795×10^6	5.365	4.276	5.950	12.59	8.955
10^{-3}	15	1.485×10^7	4.943	4.421	6.631	28.42	4.586
	20	9.805×10^6	5.185	4.440	6.872	24.13	6.622
	25	7.694×10^6	5.394	4.441	7.108	21.18	9.235
10^{-4}	15	1.451×10^7	4.945	4.475	7.754	45.87	4.521
	20	9.696×10^6	5.192	4.493	8.050	38.83	6.608
	25	7.625×10^6	5.400	4.497	8.333	34.17	9.202
10^{-5}	15	1.429×10^7	4.950	4.513	9.107	74.64	4.469
	20	9.578×10^6	5.197	4.531	9.521	64.61	6.519
	25	7.540×10^6	5.404	4.536	9.831	56.41	9.100
10^{-6}	15	1.398×10^7	4.959	4.549	10.82	125.6	4.409
	20	9.401×10^6	5.200	4.567	11.25	107.4	6.426
	25	7.423×10^6	5.407	4.571	11.63	94.03	8.984
10^{-7}	15	1.343×10^7	4.964	4.581	12.47	192.1	4.424
	20	9.111×10^6	5.199	4.598	12.82	159.5	6.389
	25	7.231×10^6	5.405	4.600	13.08	134.2	8.926
0	15	1.033×10^7	4.966	4.585	12.58	195.9	4.468
	20	7.718×10^6	5.192	4.607	12.87	162.3	6.316
	25	6.427×10^6	5.399	4.608	13.10	135.5	8.829

Table 7: Properties of models with varying mass and metallicity during He burning stage.

Z	M (M_{\odot})	Star Age (yr)	$\log(L/L_{\odot})$	$\log T_{\text{eff}}$ (K)	T_c^a (10^7 K)	ρ_c^b (g cm $^{-3}$)	M_{α}^c (M_{\odot})	$M_{C/O}^d$ (M_{\odot})	M_{cc}^e (M_{\odot})
Helium Ignition									
Z_{\odot}	15	1.584×10^7	5.127	3.503	16.79	715	6.104	0.000	2.772
	20	1.007×10^7	5.234	3.766	17.21	547	8.020	0.000	4.420
	25	7.812×10^6	5.435	3.642	17.57	435	10.61	0.000	6.551
	10^{-3}	1.487×10^7	5.015	3.764	17.47	797	6.271	0.000	2.381
	20	9.822×10^6	5.256	4.192	18.09	610	8.702	0.000	3.670
	25	7.708×10^6	5.449	4.234	18.64	492	11.78	0.000	5.729
	10^{-4}	1.453×10^7	5.022	4.316	17.53	785	6.227	0.000	2.240
	20	9.712×10^6	5.278	4.429	18.14	606	8.214	0.000	3.707
	25	7.638×10^6	5.476	4.449	18.67	492	11.04	0.000	5.750
10^{-5}	15	1.431×10^7	4.984	4.443	17.54	741	6.215	0.000	2.240
	20	9.592×10^6	5.217	4.503	18.18	566	8.718	0.000	3.826
	25	7.551×10^6	5.425	4.531	18.71	458	11.75	0.000	6.048
	10^{-6}	1.399×10^7	4.981	4.546	17.60	679	6.227	0.000	2.526
	20	9.413×10^6	5.224	4.581	18.27	529	8.583	0.000	4.385
	25	7.432×10^6	5.433	4.591	18.87	440	11.55	0.000	6.953
	10^{-7}	1.344×10^7	4.999	4.596	17.89	635	6.125	0.000	3.206
	20	9.121×10^6	5.228	4.616	18.52	520	8.557	0.000	5.145
	25	7.239×10^6	5.430	4.619	19.05	439	11.41	0.000	7.596
0	15	1.034×10^7	5.008	4.604	18.05	631	6.199	0.000	3.505
	20	7.727×10^6	5.223	4.627	18.57	523	8.407	0.000	5.199
	25	6.436×10^6	5.424	4.628	19.07	441	11.37	0.000	7.612
Helium Exhaustion									
Z_{\odot}	15	1.663×10^7	5.156	3.502	30.32	2779	7.116	5.315	4.421
	20	1.074×10^7	5.271	3.510	31.01	2491	8.609	6.674	5.696
	25	8.359×10^6	5.452	3.511	31.84	2140	11.24	9.147	8.005
	10^{-3}	1.565×10^7	5.175	3.580	30.57	2741	7.341	5.596	4.625
	20	1.044×10^7	5.321	3.591	31.31	2348	9.454	7.503	6.466
	25	8.219×10^6	5.505	3.590	32.13	2025	12.38	10.24	9.047
	10^{-4}	1.532×10^7	5.160	3.617	30.46	2741	7.208	5.479	4.552
	20	1.035×10^7	5.345	4.080	31.25	2409	9.039	7.109	6.090
	25	8.164×10^6	5.527	4.116	32.05	2088	11.72	9.529	8.376
10^{-5}	15	1.505×10^7	5.133	3.927	30.51	2751	7.110	5.500	4.493
	20	1.018×10^7	5.326	3.617	31.30	2296	9.472	7.725	6.573
	25	8.041×10^6	5.543	3.615	32.14	1988	12.43	10.49	9.188
10^{-6}	15	1.471×10^7	5.119	4.180	30.39	2757	6.856	5.384	4.343
	20	9.983×10^6	5.323	3.914	31.37	2336	9.190	7.566	6.346
	25	7.910×10^6	5.534	3.616	32.04	1985	12.12	10.30	8.942
10^{-7}	15	1.412×10^7	5.106	4.299	30.28	2759	6.585	5.278	4.158
	20	9.668×10^6	5.316	4.123	31.08	2296	8.885	7.391	6.120
	25	7.702×10^6	5.522	3.616	32.07	2011	11.76	10.07	8.581
0	15	1.099×10^7	5.094	4.407	30.07	2687	6.304	5.260	4.091
	20	8.263×10^6	5.299	4.314	31.18	2338	8.510	7.256	5.926
	25	6.893×10^6	5.498	4.008	31.91	1988	11.41	9.927	8.460

Table 8: Properties of models with varying mass and metallicity during C burning stage.

Z	M_{\odot} (M_{\odot})	Star Age (yr)	$\log(L/L_{\odot})$	$\log T_{\text{eff}}$ (K)	T_c^a (10^7 K)	ρ_c^b (g cm $^{-3}$)	M_{α}^c (M_{\odot})	$M_{C/O}^d$ (M_{\odot})	$M_{O/Ne}^e$ (M_{\odot})	M_{ec}^f (M_{\odot})
Carbon Ignition										
Z_{\odot}	15	1.644×10^7	5.261	3.493	52.43	17780	7.122	5.315	0.000	0.000
	20	1.075×10^7	5.362	3.501	55.45	17420	8.611	6.674	0.000	0.000
	25	8.366×10^6	5.557	3.501	61.84	20130	11.24	9.147	0.000	0.000
10^{-3}	15	1.566×10^7	5.299	3.567	84.06	1.271×10^5	7.358	5.600	0.000	0.000
	20	1.045×10^7	5.450	3.572	97.57	4.047×10^5	9.454	7.457	0.800	0.000
	25	8.226×10^6	5.627	3.574	115.7	6.101×10^5	12.38	9.963	1.822	0.000
10^{-4}	15	1.533×10^7	5.275	3.607	84.04	1.319×10^5	7.212	5.483	0.000	0.224
	20	1.037×10^7	5.380	3.613	89.47	1.210×10^5	9.053	7.111	0.000	0.353
	25	8.172×10^6	5.501	3.620	101.8	3.322×10^5	11.67	9.333	1.024	0.000
10^{-5}	15	1.507×10^7	5.273	3.611	83.56	1.273×10^5	7.115	5.504	0.000	0.235
	20	1.019×10^7	5.496	3.609	99.78	4.306×10^5	9.493	7.676	1.007	0.000
	25	8.049×10^6	5.669	3.610	98.05	2.243×10^5	12.44	10.37	0.761	0.000
10^{-6}	15	1.473×10^7	5.254	3.612	82.85	1.270×10^5	6.881	5.390	0.000	0.224
	20	9.993×10^6	5.451	3.611	83.29	1.077×10^5	9.216	7.568	0.000	0.445
	25	7.918×10^6	5.595	3.612	93.00	1.440×10^5	12.14	10.26	0.221	0.000
10^{-7}	15	1.414×10^7	5.239	3.612	79.56	1.261×10^5	6.604	5.285	0.000	0.065
	20	9.679×10^6	5.425	3.611	82.76	1.056×10^5	8.874	7.394	0.000	0.002
	25	7.710×10^6	5.575	3.613	109.8	4.675×10^5	11.77	9.985	1.391	0.000
$Z = 0$	15	1.100×10^7	5.013	3.656	82.81	41.225×10^5	6.313	5.268	0.000	0.289
	20	8.273×10^6	5.184	3.624	114.2	3.876×10^5	8.521	7.262	1.540	0.000
	25	6.902×10^6	5.568	3.613	110.8	4.780×10^5	11.59	9.931	1.463	0.000
Carbon Exhaustion										
Z_{\odot}	15	1.664×10^7	5.289	3.490	107.3	6.274×10^5	7.125	5.319	1.210	0.000
	20	1.075×10^7	5.407	3.497	111.6	5.233×10^5	8.611	6.573	1.363	0.000
	25	8.367×10^6	5.558	3.501	109.8	6.182×10^5	11.24	8.924	1.249	0.000
10^{-3}	15	1.566×10^7	5.303	3.567	108.0	5.925×10^5	7.358	5.600	1.264	0.000
	20	1.045×10^7	5.450	3.572	115.8	8.937×10^5	9.454	7.431	2.283	0.000
	25	8.226×10^6	5.627	3.574	115.7	6.101×10^5	12.38	9.963	1.822	0.000
10^{-4}	15	1.533×10^7	5.277	3.607	107.4	6.036×10^5	7.212	5.484	1.224	0.000
	20	1.037×10^7	5.391	3.612	112.6	4.902×10^5	9.053	7.030	1.375	0.000
	25	8.172×10^6	5.501	3.620	114.2	6.334×10^5	11.67	9.290	1.543	0.000
10^{-5}	15	1.507×10^7	5.276	3.610	107.9	6.126×10^5	7.115	5.505	1.251	0.000
	20	1.019×10^7	5.495	3.609	114.5	9.300×10^5	9.528	7.655	2.606	0.000
	25	8.049×10^6	5.628	3.609	115.1	6.309×10^5	13.06	10.37	1.717	0.000
10^{-6}	15	1.473×10^7	5.236	3.612	106.4	7.067×10^5	7.350	5.390	1.244	0.000
	20	9.993×10^6	5.458	3.574	113.8	4.516×10^5	9.030	7.571	1.458	0.000
	25	7.918×10^6	5.472	3.546	110.9	6.655×10^5	10.46	10.26	1.357	0.000
10^{-7}	15	1.414×10^7	5.328	3.532	106.0	6.778×10^5	5.506	5.285	1.200	0.000
	20	9.679×10^6	5.393	3.500	111.0	5.416×10^5	7.318	7.318	1.351	0.000
	25	7.710×10^6	5.575	3.613	107.7	5.534×10^5	11.77	9.950	1.201	0.000
0	15	1.100×10^7	5.027	3.622	105.9	7.585×10^5	5.317	5.273	1.265	0.000
	20	8.273×10^6	5.336	3.608	108.5	4.122×10^5	7.484	7.246	1.540	0.000
	25	6.902×10^6	5.568	3.613	108.6	5.477×10^5	11.59	9.931	1.276	0.000

Table 9: Properties of models with varying mass and metallicity during O burning stage.

Z	M_\odot (M_\odot)	Star Age (yr)	$\log(L/L_\odot)$	$\log T_{\text{eff}}$ (K)	T_c^a (10^7 K)	ρ_c^b (g cm $^{-3}$)	M_α^c (M_\odot)	$M_{C/O}^d$ (M_\odot)	$M_{O Ne}^e$ (M_\odot)	M_{cc}^f (M_\odot)
Oxygen Ignition										
Z_\odot	15	1.664×10^7	5.288	3.490	160.2	1.056×10^7	7.125	5.290	4.889	0.000
	20	1.075×10^7	5.404	3.497	176.4	2.674×10^6	8.610	6.563	5.088	0.000
	25	8.367×10^6	5.558	3.501	184.0	1.743×10^6	11.24	8.426	3.659	0.000
10^{-3}	15	1.566×10^7	5.304	3.567	155.5	1.028×10^7	7.357	5.570	5.233	0.000
	20	1.045×10^7	5.452	3.572	156.3	6.554×10^6	9.454	7.248	1.736	0.000
	25	8.226×10^6	5.627	3.574	183.4	2.162×10^6	12.38	9.911	3.797	0.000
10^{-4}	15	1.533×10^7	5.277	3.607	152.8	4.251×10^6	7.212	5.414	4.794	0.000
	20	1.037×10^7	5.390	3.612	179.0	2.567×10^6	9.052	6.947	5.289	0.002
	25	8.172×10^6	5.501	3.620	184.8	1.836×10^6	11.67	9.218	4.150	0.000
10^{-5}	15	1.507×10^7	5.276	3.610	156.9	1.007×10^7	7.115	5.469	5.091	0.000
	20	1.019×10^7	5.526	3.609	159.7	4.434×10^6	9.993	7.634	2.023	0.000
	25	8.049×10^6	5.691	3.611	183.0	1.901×10^6	13.06	10.37	5.787	0.000
10^{-6}	15	1.473×10^7	5.226	3.611	187.4	5.375×10^6	7.091	5.390	4.997	0.332
	20	9.993×10^6	5.418	3.571	177.2	2.770×10^6	8.710	7.571	2.941	0.003
	25	7.918×10^6	5.468	3.545	180.2	1.758×10^6	10.44	10.26	3.139	0.000
10^{-7}	15	1.414×10^7	5.313	3.534	153.0	1.255×10^7	5.511	5.285	5.054	0.000
	20	9.679×10^6	5.385	3.501	161.1	2.988×10^6	7.318	7.318	1.829	0.000
	25	7.710×10^6	5.594	3.612	72.11	4.378×10^4	11.77	10.07	0.000	0.000
0	15	1.100×10^7	5.093	3.520	152.2	1.310×10^7	5.310	5.273	4.990	0.000
	20	8.273×10^6	5.321	3.614	173.2	3.387×10^6	7.473	7.246	6.405	0.000
	25	6.902×10^6	5.866	3.592	160.0	8.022×10^6	10.27	9.868	9.283	0.000
Oxygen Exhaustion										
Z_\odot	15	1.664×10^7	5.288	3.490	250.0	9.775×10^6	7.124	5.271	4.896	0.000
	20	1.075×10^7	5.405	3.497	251.8	9.490×10^6	8.610	6.556	6.226	0.000
	25	8.367×10^6	5.570	3.504	261.9	1.046×10^7	11.29	4.814	2.839	0.000
10^{-3}	15	1.566×10^7	5.302	3.567	250.0	1.184×10^7	7.357	5.570	5.255	0.000
	20	1.045×10^7	5.449	3.573	216.7	4.679×10^7	9.454	7.437	7.419	0.000
	25	8.226×10^6	5.627	3.574	258.6	1.068×10^7	12.38	9.910	9.729	0.000
10^{-4}	15	1.533×10^7	5.277	3.607	250.9	1.247×10^7	7.211	5.415	5.146	0.000
	20	1.037×10^7	5.423	3.614	253.1	1.005×10^7	9.119	6.947	6.591	0.000
	25	8.172×10^6	5.489	3.620	226.0	3.193×10^7	11.58	9.092	2.306	0.000
10^{-5}	15	1.507×10^7	5.276	3.611	251.9	1.008×10^7	7.115	5.469	5.097	0.000
	20	1.019×10^7	5.532	3.606	228.5	3.346×10^7	10.01	7.634	1.895	0.000
	25	8.049×10^6	5.713	3.605	243.8	1.519×10^7	13.06	10.37	10.29	0.000
10^{-6}	15	1.473×10^7	5.227	3.611	249.1	1.069×10^7	7.091	5.390	5.003	0.000
	20	9.993×10^6	5.423	3.571	241.4	1.088×10^7	8.489	7.571	7.211	0.000
	25	7.918×10^6	5.468	3.545	254.6	1.055×10^7	10.44	10.26	2.419	0.000
10^{-7}	15	1.414×10^7	5.316	3.533	237.8	4.074×10^7	5.511	5.285	5.060	0.000
	20	9.679×10^6	5.389	3.501	219.7	1.871×10^7	7.318	7.318	7.029	0.000
0	15	1.100×10^7	5.100	3.519	212.8	1.845×10^7	5.310	5.272	5.013	0.000
	20	8.273×10^6	5.325	3.615	231.1	3.003×10^7	7.473	7.246	7.083	0.000
	25	6.902×10^6	5.859	3.587	253.2	1.123×10^7	10.27	9.868	9.430	0.000

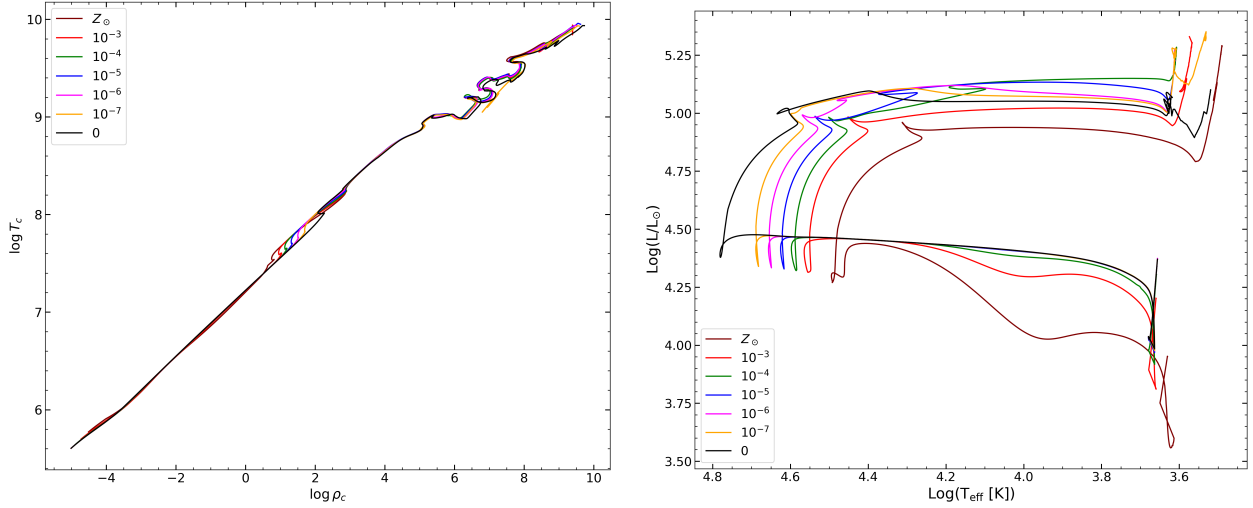


Figure 9: Core and Surface evolution for the 15M models with various metallicities.

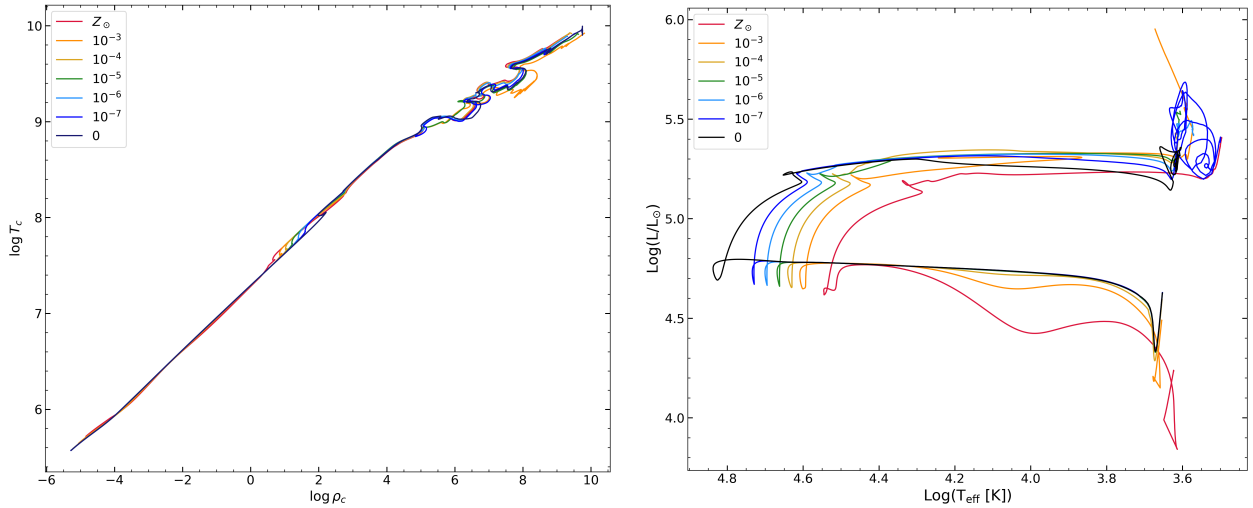


Figure 10: Core and Surface evolution for the 20M models with various metallicities.

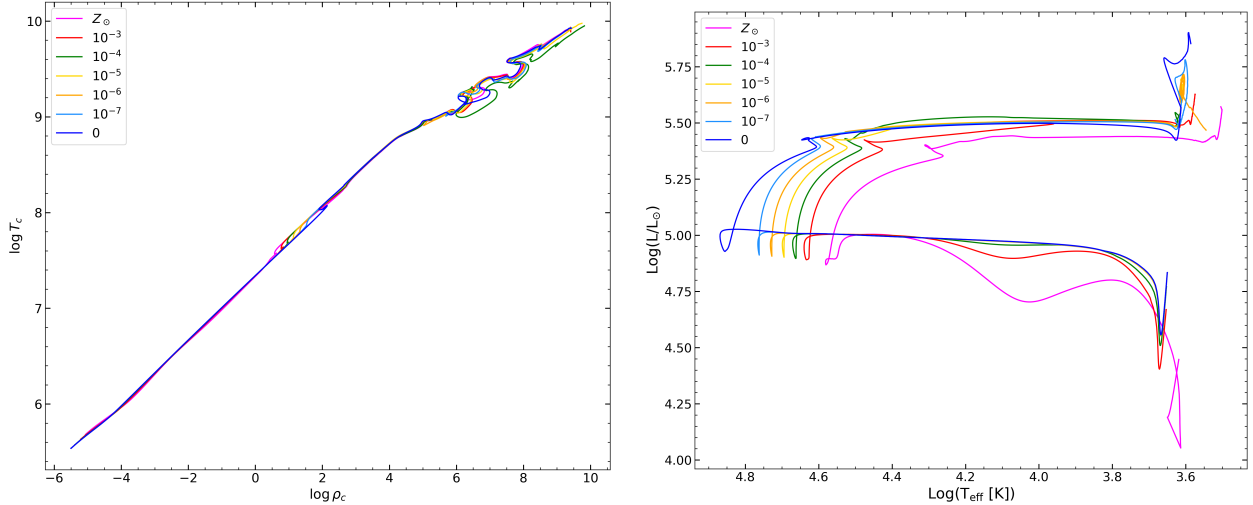


Figure 11: Core and Surface evolution for the 25M models with various metallicities.

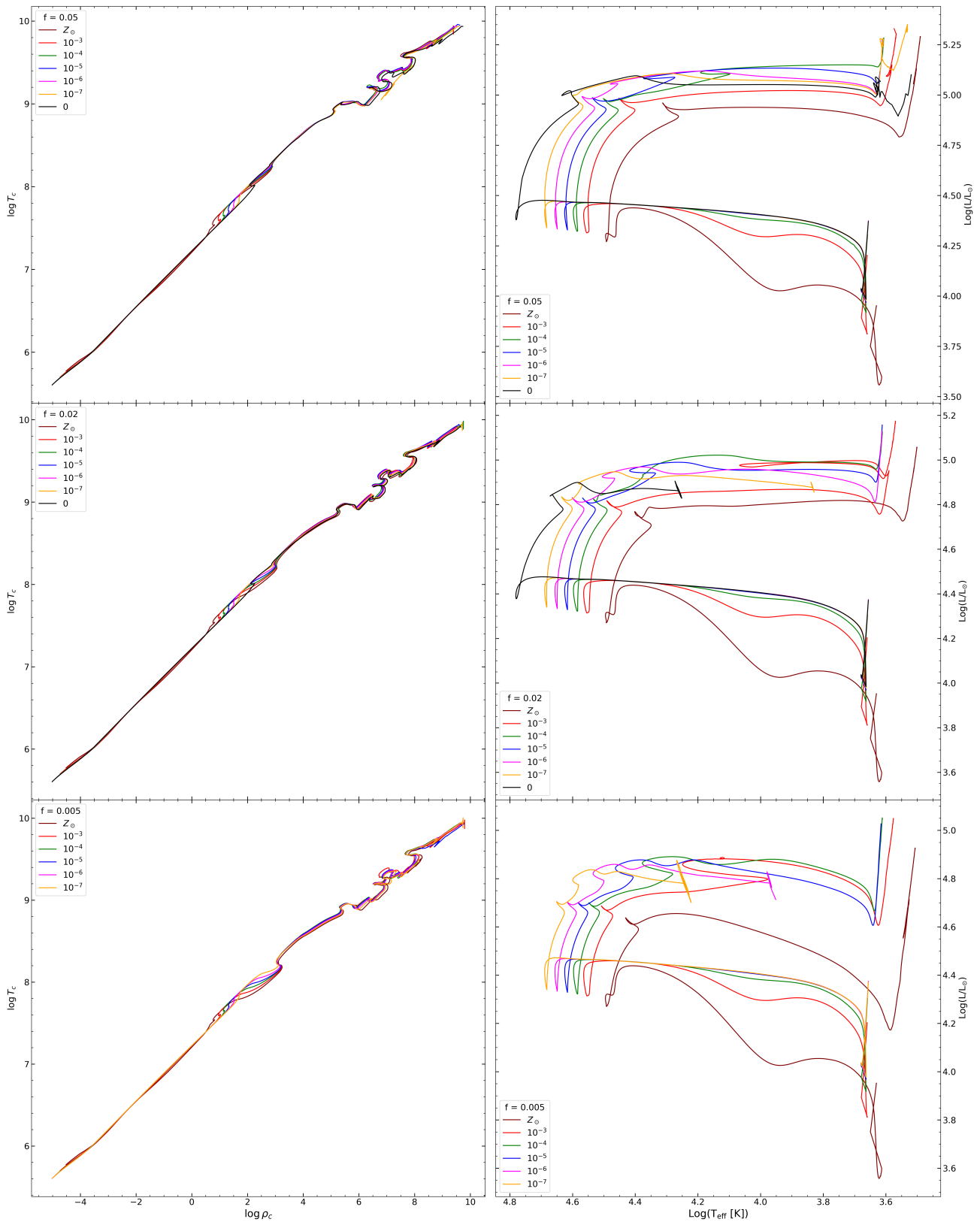


Figure 12: Core and surface evolution for the 15M models at different CBM factors.

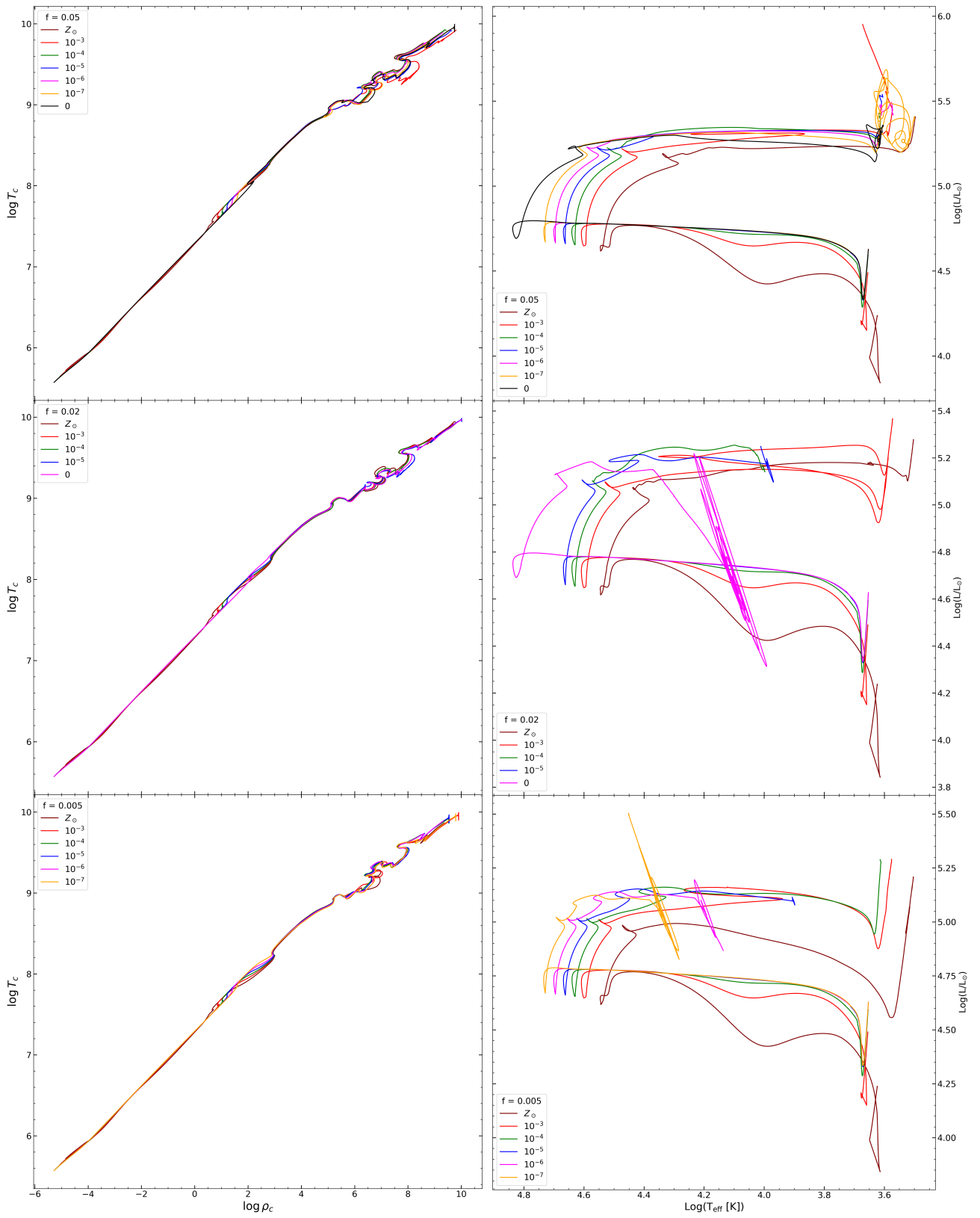


Figure 13: Core and surface evolution for the 20M models at different CBM factors.

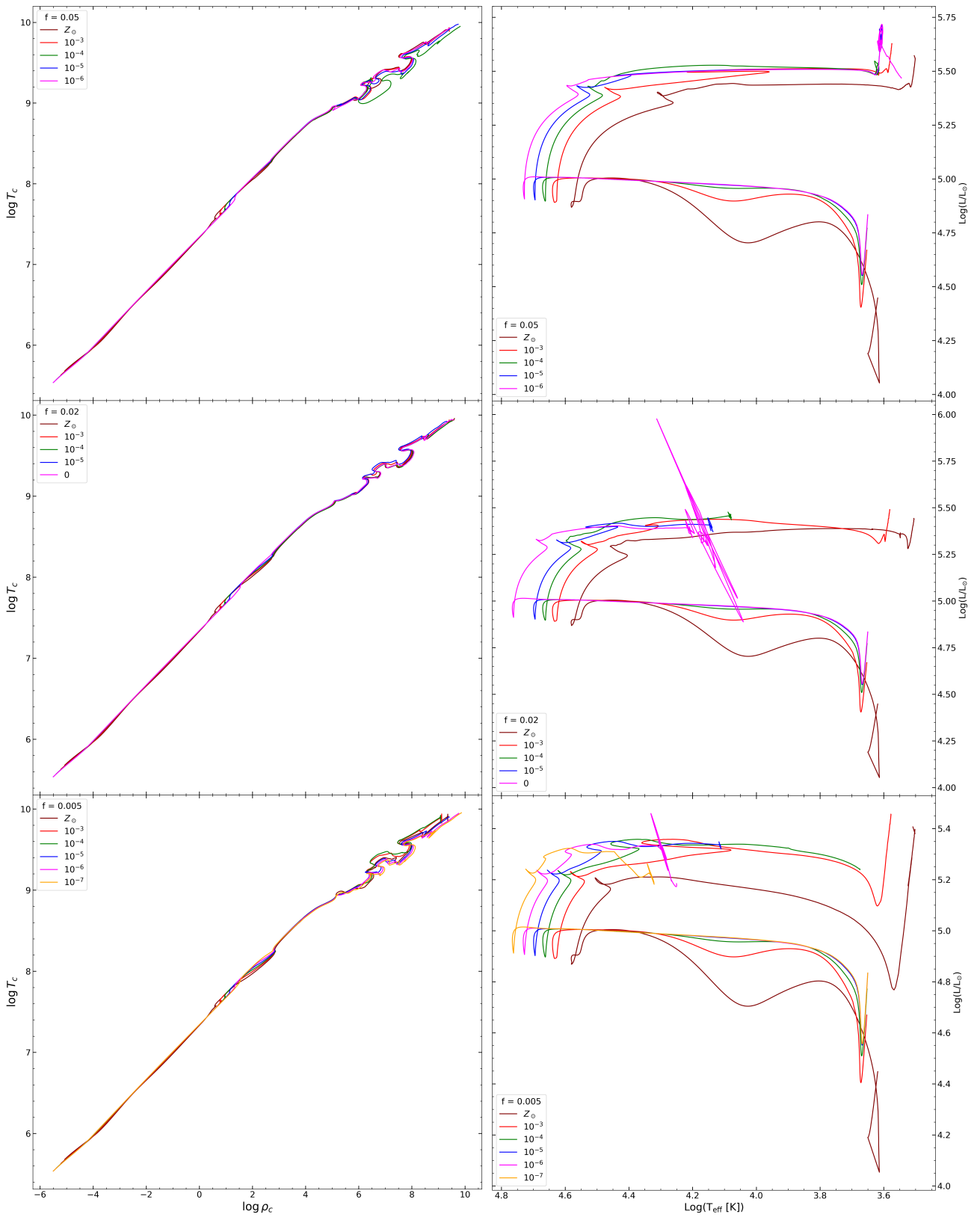


Figure 14: Core and surface evolution for the $25M$ models at different CBM factors.

5 Pre-Supernova Abundance

While nucleosynthesis takes place throughout a star's lifetime, this section focuses on the final abundance profiles at core collapse. Mass fraction and yield plots are presented for key isotopes— ^{12}C , ^{14}N , and ^{16}O —across our model grid, which spans different metallicities and CBM rates. These final-stage abundance patterns encapsulate the cumulative effects of nuclear network selection, metallicity, and mixing processes on stellar evolution, and they provide critical insight into the chemical yields that contribute to the enrichment of the interstellar medium.

5.1 ^{12}C Yields and Mass Fractions

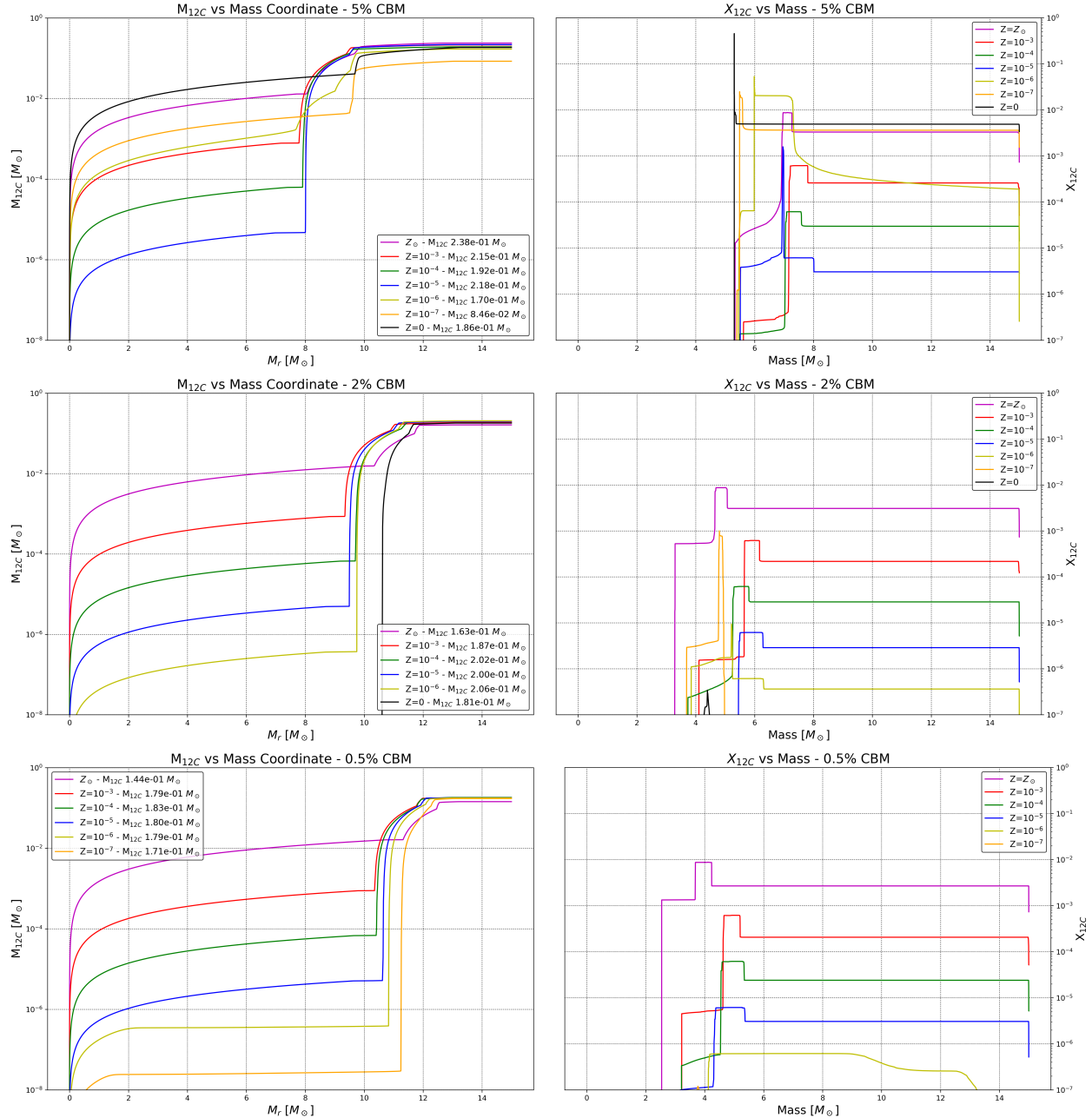


Figure 15: Comparison of ^{12}C Mass Yield (left) and Mass Fraction (right) for a $15M_\odot$ model at various metallicities, categorised by CBM Rates.

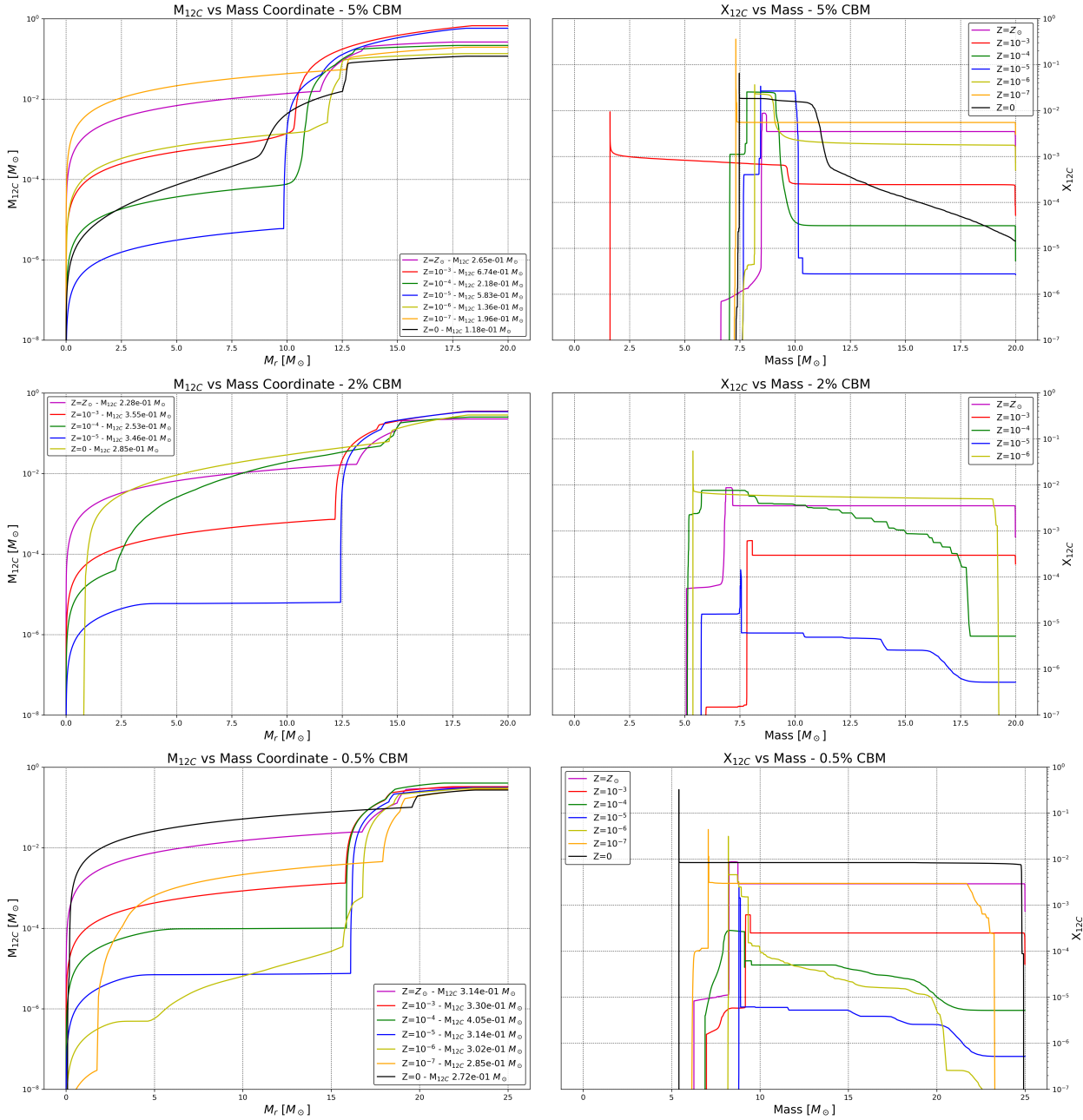


Figure 16: Comparison of ^{12}C Mass Yield (left) and Mass Fraction (right) for a $20M_{\odot}$ model at various metallicities, categorised by CBM Rates.

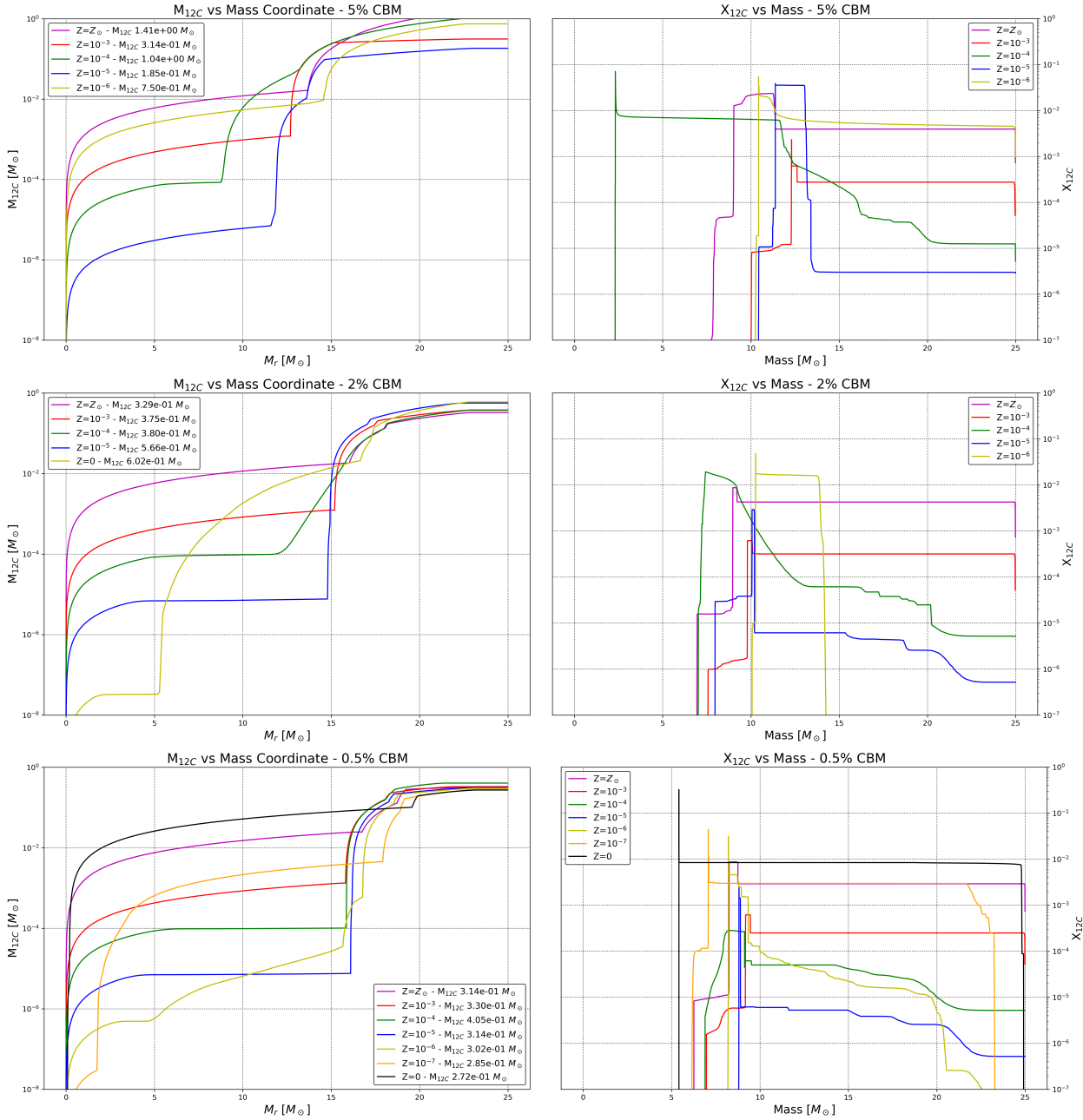


Figure 17: Comparison of ^{12}C Mass Yield (left) and Mass Fraction (right) for a $25M_{\odot}$ model at various metallicities, categorised by CBM Rates.

5.2 ^{14}N Yields and Mass Fractions

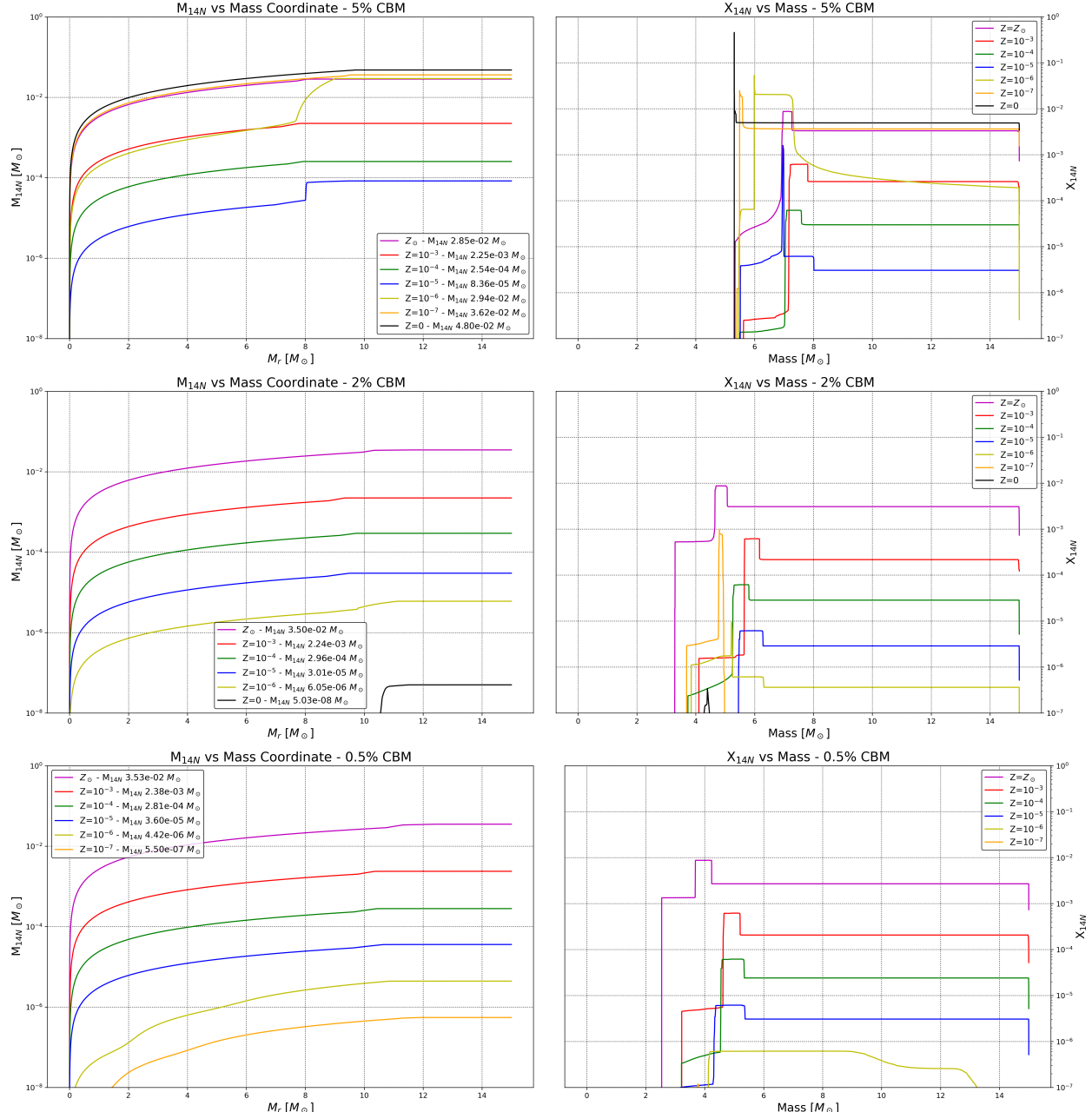


Figure 18: Comparison of ^{14}N Mass Yield (left) and Mass Fraction (right) for a $15M_\odot$ model at various metallicities, categorised by CBM Rates.

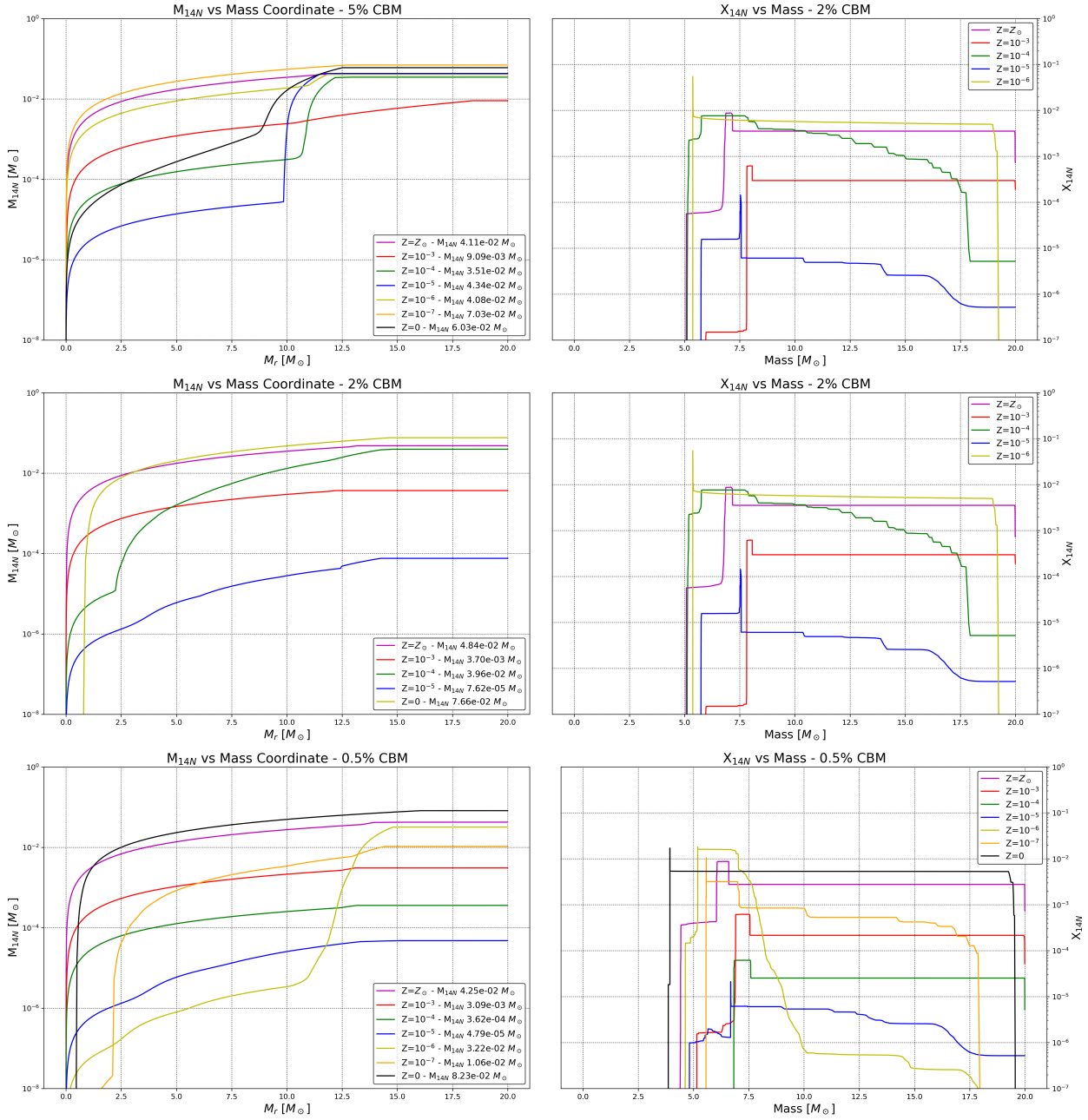


Figure 19: Comparison of ^{14}N Mass Yield (left) and Mass Fraction (right) for a $20M_\odot$ model at various metallicities, categorised by CBM Rates.

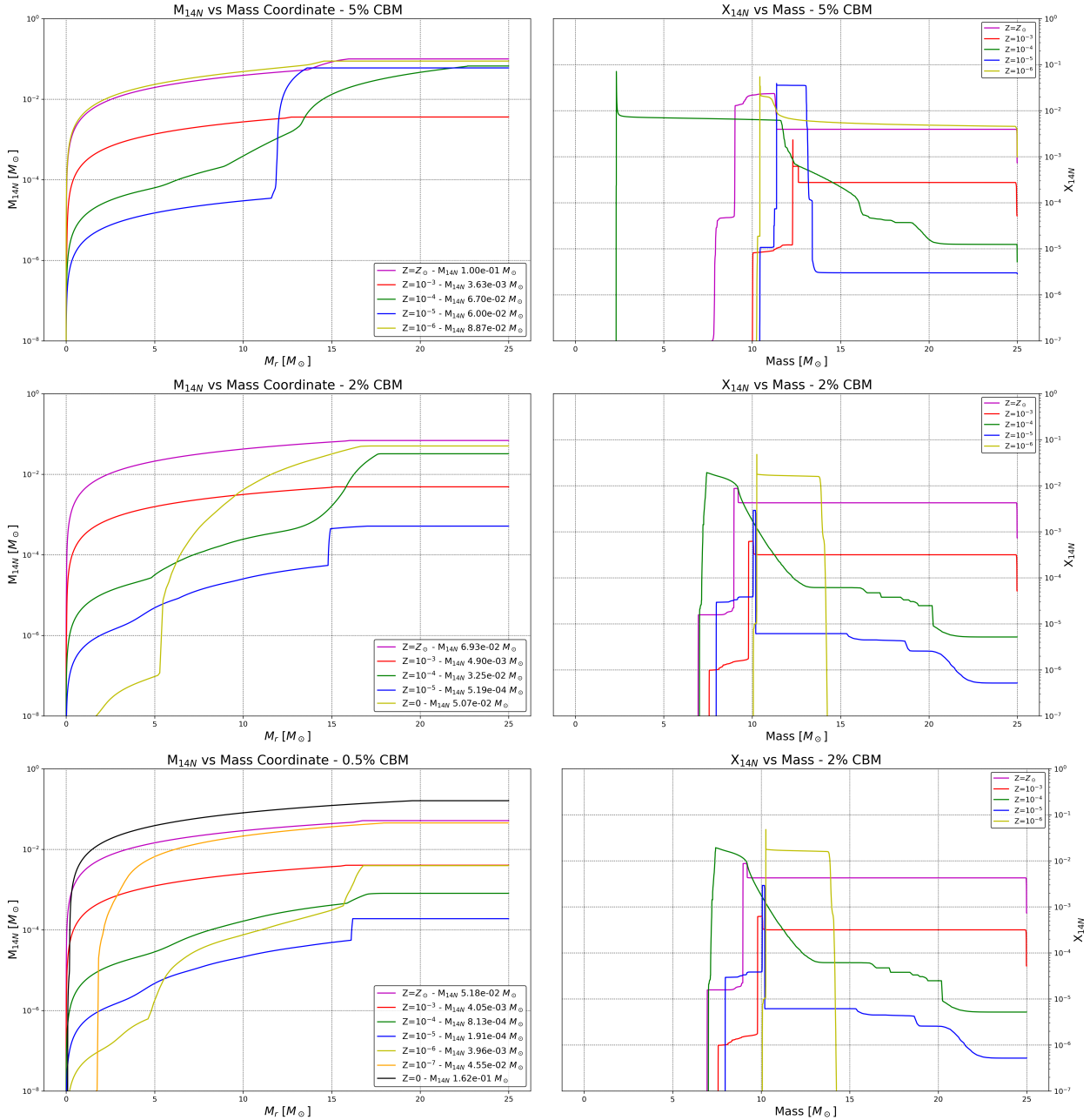


Figure 20: Comparison of ^{14}N Mass Yield (left) and Mass Fraction (right) for a $25M_{\odot}$ model at various metallicities, categorised by CBM Rates.

5.3 ^{16}O Yields and Mass Fractions

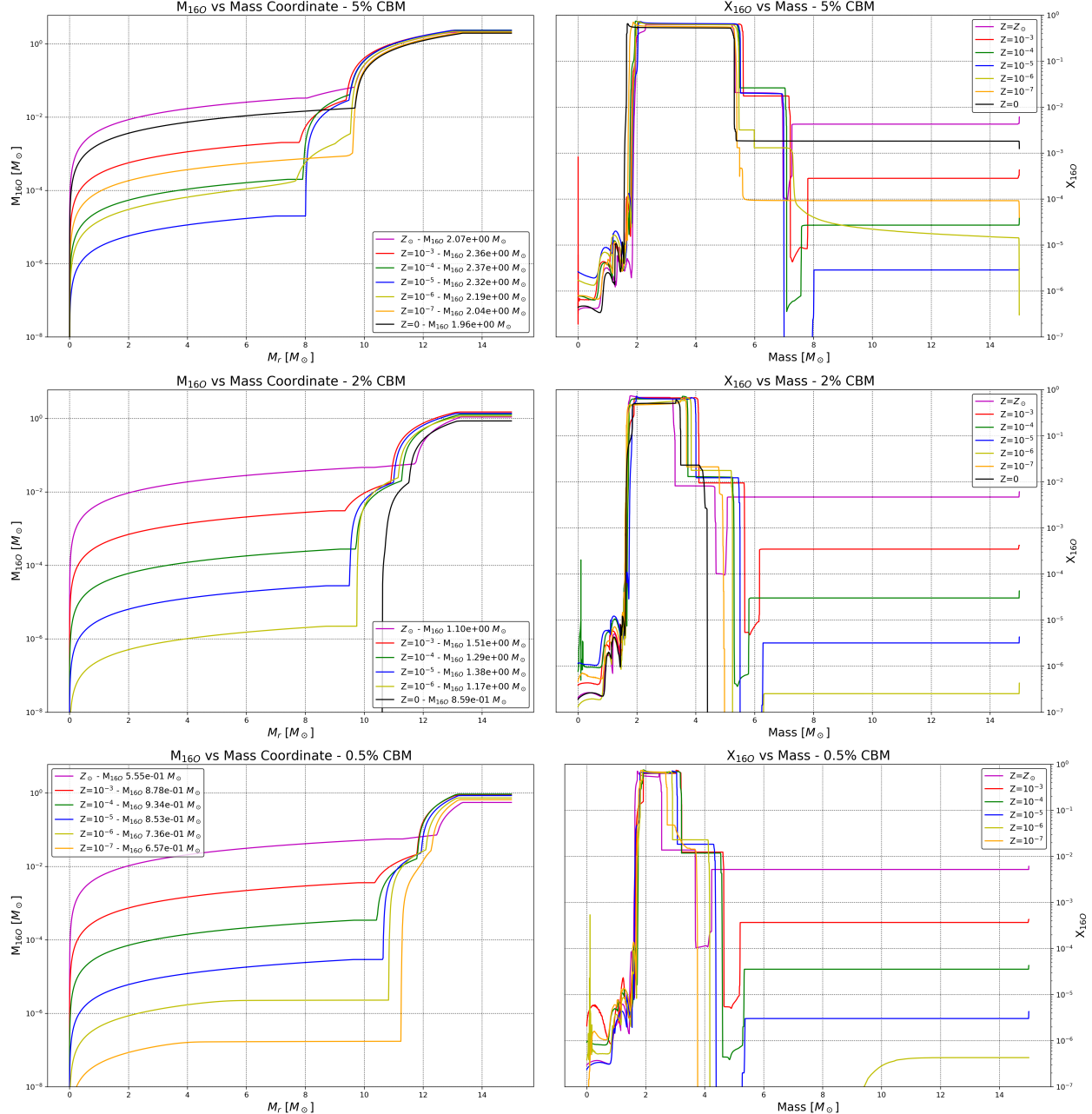


Figure 21: Comparison of ^{16}O Mass Yield (left) and Mass Fraction (right) for a $15M_{\odot}$ model at various metallicities, categorised by CBM Rates.

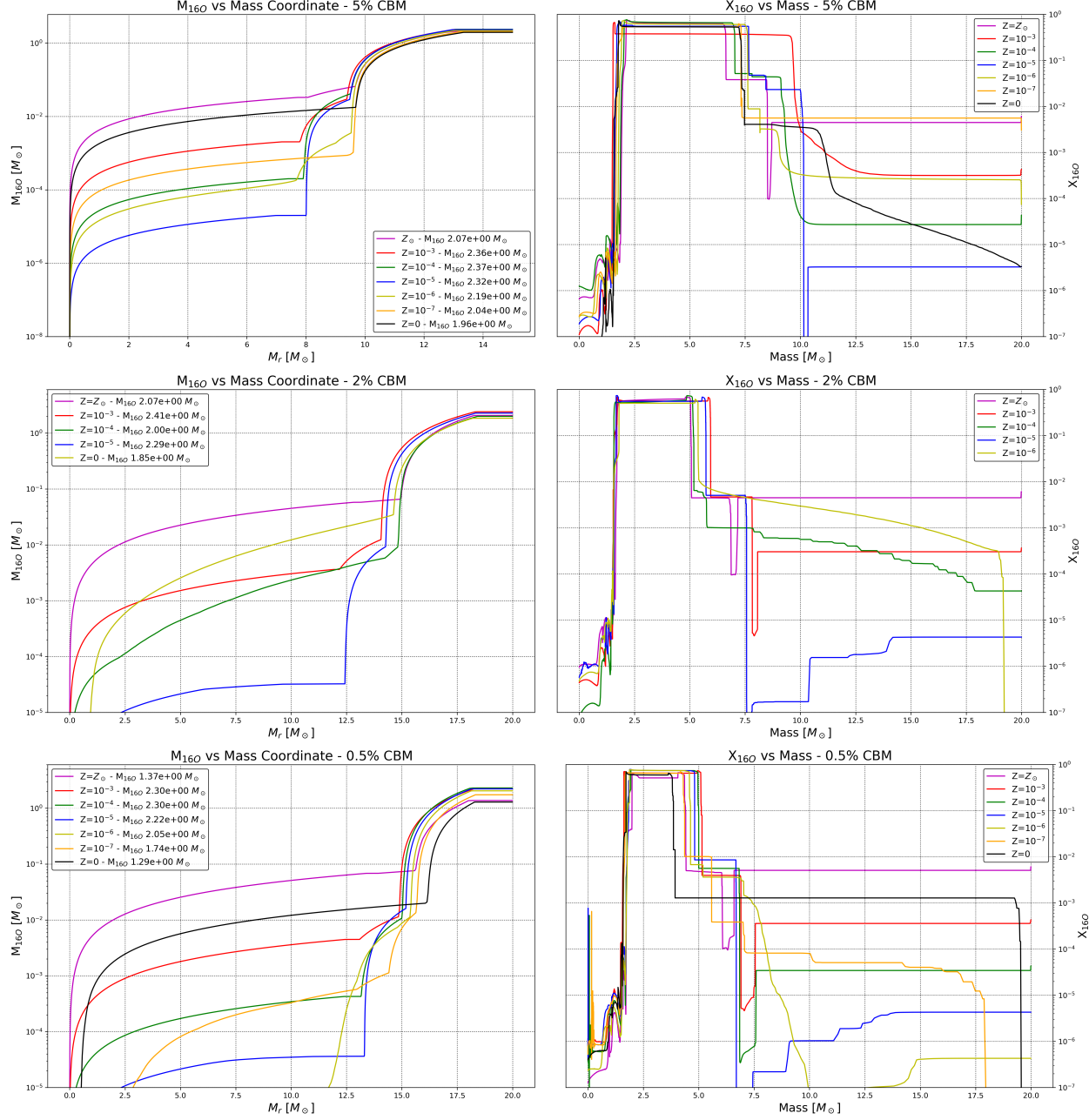


Figure 22: Comparison of ^{16}O Mass Yield (left) and Mass Fraction (right) for a 15M_\odot model at various metallicities, categorised by CBM Rates.

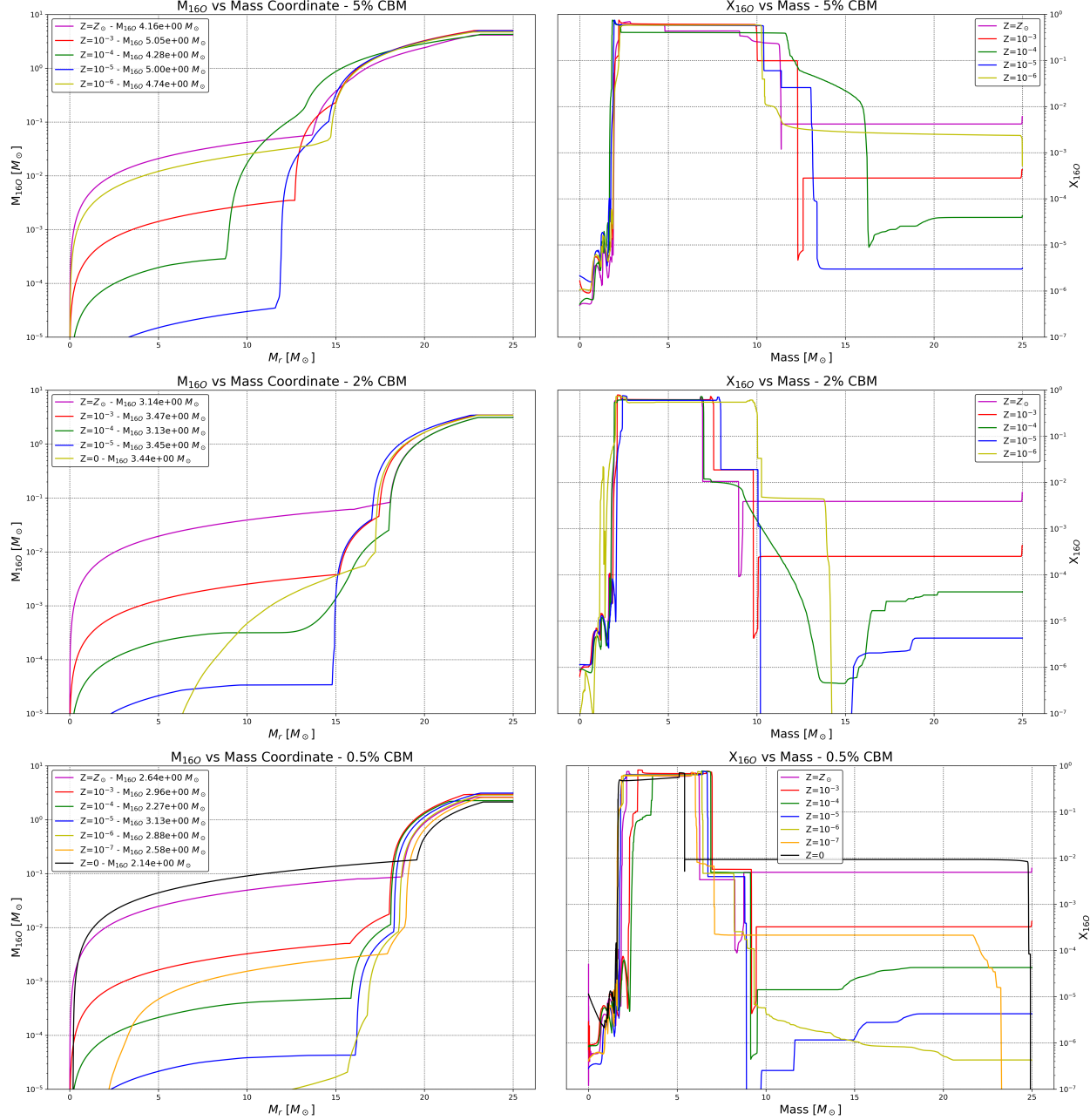


Figure 23: Comparison of ^{16}O Mass Yield (left) and Mass Fraction (right) for a 15M_\odot model at various metallicities, categorised by CBM Rates.

6 Analysis of Burning Stages

6.1 Across Nuclear Networks

The nuclear burning sequence of a massive star follows a well-defined progression, where hydrogen, helium, carbon, and heavier elements fuse in successive stages. Each burning phase leaves behind ashes that serve as fuel for the next stage, ultimately determining the star's final fate. The core temperature (T_c) and density (ρ_c) dictate the nuclear reaction rates, while convection plays a critical role in mixing newly synthesized elements throughout the star.

This section examines the impact of different nuclear networks on a $20M_\odot$ model at solar metallicity ($Z = Z_\odot$), using four networks: `approx21` (A21), `o_burn_full` (OB), `mesa_128` (M128), and `mesa_206` (M206). The Kippenhahn plots in Figure 7 provide a visualization of convective and radiative zones over time, while Figure 5 traces their evolution in the Hertzsprung-Russell (HR) diagram. These models are compared at key evolutionary stages: main sequence, hydrogen and helium exhaustion, and carbon ignition.

6.1.1 Main Sequence and Hydrogen Burning

The star enters the main sequence phase with a convective hydrogen-burning core, where the CNO cycle dominates energy production. Initially, all networks exhibit similar conditions, with $\log L/L_\odot = 4.630$ and $\log T_{\text{eff}} = 4.545$. The core temperature and density at the start of hydrogen burning are approximately $T_c = 7.562 \times 10^7$ K and $\rho_c = 0.711 \text{ g cm}^{-3}$ across all networks. However, the size of the convective core varies slightly due to differences in reaction rates **A21**: $M_{\text{conv,H}} = 8.20M_\odot$, **OB**: $M_{\text{conv,H}} = 7.61M_\odot$, **M128**: $M_{\text{conv,H}} = 7.80M_\odot$, **M206**: $M_{\text{conv,H}} = 7.85M_\odot$. These differences influence the available hydrogen fuel, affecting the duration of core hydrogen burning. The OB network, with the smallest convective core, leads to a shorter main sequence lifetime compared to A21, which has the largest hydrogen-burning core.

6.1.2 Transition to Helium Burning

As core hydrogen depletes, the star leaves the main sequence and contracts, increasing the core temperature until helium burning ignites. Helium burning occurs primarily through the triple-alpha process, where three helium nuclei (${}^4\text{He}$) combine to form carbon (${}^{12}\text{C}$), with a small fraction further converted into oxygen (${}^{16}\text{O}$). The convective helium core mass at ignition follows a similar trend to the hydrogen-burning phase: **A21**: $M_{\text{conv,He}} = 6.90M_\odot$, **OB**: $M_{\text{conv,He}} = 7.23M_\odot$, **M128**: $M_{\text{conv,He}} = 8.19M_\odot$, **M206**: $M_{\text{conv,He}} = 8.20M_\odot$. The OB network exhibits the largest helium core due to its extended convective mixing, while A21 retains a slightly smaller core mass. This variation has direct implications for later burning stages, as a larger helium core produces more carbon and oxygen, affecting carbon ignition conditions.

6.1.3 Carbon Ignition and Late Burning Stages

Once helium is exhausted, carbon burning initiates when T_c exceeds 5×10^8 K. The ignition conditions vary among networks due to differences in the C/O ratio established during helium burning. The OB and M206 networks, which produced more oxygen relative to carbon, require slightly higher temperatures to ignite carbon burning compared to A21. The temperatures at carbon ignition are: **A21**: $T_c = 6.016 \times 10^8$ K, **OB**: $T_c = 8.269 \times 10^8$ K, **M128**: $T_c = 8.607 \times 10^8$ K, **M206**: $T_c = 8.700 \times 10^8$ K. Notably, the OB and M206 networks reach carbon ignition significantly earlier than A21, due to a higher accumulation of oxygen. The presence of an extended convective carbon-burning shell in OB and M206 suggests that additional mixing enhances fuel consumption, potentially delaying neon and oxygen ignition.

6.1.4 Impact on Final Evolutionary Pathways

The differences in nuclear networks lead to variations in the final core composition, influencing whether the star collapses into a neutron star or a black hole. The total carbon-oxygen (CO) core mass at oxygen exhaustion is a critical factor: **A21**: $M_{\text{CO}} = 6.91M_\odot$, **OB**: $M_{\text{CO}} = 7.23M_\odot$, **M128**: $M_{\text{CO}} = 8.20M_\odot$, **M206**: $M_{\text{CO}} = 8.20M_\odot$. Stars with CO cores exceeding $7 - 8M_\odot$ are strong candidates for direct black hole formation, while those with smaller cores may explode as supernovae, leaving behind neutron star remnants.

6.2 Across Metallicity and Mass

The nuclear burning stages in massive stars are deeply influenced by initial mass and metallicity (Z). Tables 6, 7, 8, and 9 outline the key evolutionary milestones—hydrogen (H), helium (He), carbon (C), and oxygen (O) ignition and exhaustion—across different metallicities and masses. The variations in ignition temperatures, densities, core masses, and evolutionary timescales highlight the effects of mass loss, opacity, and nuclear burning efficiency on a star’s fate.

6.2.1 Hydrogen and Helium Burning: Foundations for Later Evolution

Hydrogen burning, primarily via the CNO cycle in massive stars, dominate the main sequence lifetime. The onset of H burning is relatively uniform across different metallicities, but the duration of core H burning is strongly dependent on metallicity.

At solar metallicity ($Z = Z_\odot$), stars maintain a relatively extended main sequence phase due to increased opacity from metals, which slows core contraction. In contrast, metal-poor ($Z = 10^{-4} - 10^{-7}$) and metal-free ($Z = 0$) stars experience more efficient radiative energy loss, causing more rapid H exhaustion. This leads to shorter main sequence lifetimes and higher core densities at the end of H burning.

Impact of Mass on H Burning: Higher-mass models (20 and $25M_\odot$) sustain larger convective cores due to their stronger temperature sensitivity to the CNO cycle. For instance, at $Z = Z_\odot$, the H-burning convective core masses are: $M_{\text{conv,H}} = 6.70M_\odot$ for $15M_\odot$, $M_{\text{conv,H}} = 8.94M_\odot$ for $20M_\odot$, $M_{\text{conv,H}} = 11.20M_\odot$ for $25M_\odot$. As mass increases, higher central temperatures (T_c) and densities (ρ_c) allow for more efficient H fusion, extending core burning phases.

Helium Burning Transition: When H is exhausted, the core contracts, increasing T_c until He fusion begins via the triple-alpha process. The ignition conditions of He burning exhibit clear trends:

- Metal-poor stars have higher core densities at He ignition, as lower opacities lead to more compact structures.
- Higher-mass models transition smoothly from H to He burning, while lower-mass models ($M = 15M_\odot$) undergo a more significant contraction before reaching He ignition conditions.
- The He core mass (M_α) at ignition increases with mass, affecting subsequent carbon formation.

For instance, at $Z = 10^{-4}$, the He core mass at ignition follows: $M_\alpha = 6.50M_\odot$ for $15M_\odot$, $8.23 M_\odot$ for $20M_\odot$ and $11.10M_\odot$ for $25M_\odot$. These variations influence the amount of carbon and oxygen available for later burning stages.

6.2.2 Carbon Burning: Influence of Metallicity and Mass

Carbon burning occurs when the core reaches $T_c \gtrsim 5 \times 10^8$ K, triggering ^{12}C fusion via $^{12}\text{C}(^{12}\text{C},\alpha)^{20}\text{Ne}$ and $^{12}\text{C}(^{12}\text{C},\text{p})^{23}\text{Na}$. The conditions for carbon ignition show systematic trends across metallicity and mass:

- Lower-metallicity ($Z \leq 10^{-4}$) stars have higher core densities at carbon ignition, facilitating earlier onset of carbon burning.
- Metal-rich stars maintain lower core densities, delaying C ignition slightly.
- The He core mass at C ignition increases with metallicity, leading to larger CO cores in later stages.

Impact of Mass: At $Z = 10^{-3}$, the C-burning core masses are: $M_{\text{CO}} = 5.60M_\odot$ for $15M_\odot$, $7.45M_\odot$ for $20M_\odot$, $9.96M_\odot$ for $25M_\odot$. This variation in CO core size influences whether a star will undergo core-collapse supernova (CCSN) or pair-instability supernova (PISN). Stars with larger CO cores ($M_{\text{CO}} > 7 - 8M_\odot$) at oxygen exhaustion are more likely to form direct black holes.

6.2.3 Oxygen Burning: The Final Hydrostatic Stage

Oxygen burning occurs when $T_c \gtrsim 1.5$ GK. The duration of this stage and the amount of synthesised silicon (^{28}Si) and iron-group elements depend on core mass and metallicity.

Key Trends at O Ignition:

- Lower-mass stars ($15M_\odot$) have shorter O-burning phases, producing less iron.
- Higher-mass stars ($\geq 25M_\odot$) sustain longer O-burning periods, generating significant amounts of silicon and iron-group elements.
- The presence of convective O-burning shells in some models suggests enhanced mixing, affecting final nucleosynthesis yields.

Core Masses at O Exhaustion:

- At $Z = Z_{\odot}$, the O-exhausted core mass is $M_O \approx 7.5 - 9.5 M_{\odot}$.
- At $Z = 10^{-6}$, the O core mass is $M_O \approx 10 - 11 M_{\odot}$, significantly larger than its metal-rich counterparts.

This confirms that metal-free and metal-poor stars retain larger CO cores, favoring direct black hole formation, while metal-rich stars with smaller CO cores are more likely to undergo iron-core collapse.

6.2.4 Final Remnant Formation and Supernovae

The core masses at exhaustion stages provide insight into remnant formation:

- Direct black hole formation: Stars with $M_{CO} > 7 - 8 M_{\odot}$ at O exhaustion likely bypass supernovae and collapse directly.
- Supernova fallback mechanisms: Some models retain significant unburned carbon at O exhaustion, suggesting fallback-accretion mechanisms could influence explosion dynamics.

6.3 Across various rates of CBM

CBM plays a crucial role in extending convective regions beyond the boundaries set by the Schwarzschild criterion, facilitating enhanced mixing of fuel into burning regions. This affects stellar lifetimes, core growth, and subsequent burning stages. While the previously discussed results primarily focus on the influence of mass and metallicity, here we explore the consequences of varying CBM prescriptions, as inferred from the central temperature-density (T_c - ρ_c) evolution and HRDs.

6.3.1 CBM and Hydrogen Burning: Core Growth and Main Sequence Evolution

The treatment of CBM strongly influences the structure and evolution of the convective hydrogen-burning core. More efficient CBM (e.g., larger overshooting or diffusive mixing) extends the convective core, increasing the amount of hydrogen available for fusion and thereby prolonging the main sequence lifetime.

Trends in the HR Diagram: Comparing the HRDs of models with different CBM prescriptions reveals that:

- Models with **strong CBM** (higher overshoot parameter) tend to evolve more slowly across the main sequence, remaining at higher luminosities for a longer duration.
- Models with **weaker CBM** (less overshooting or step-function boundary treatment) tend to leave the main sequence earlier due to a smaller hydrogen reservoir in the convective core.

For instance, models with extended CBM show:

- **Lower effective temperatures** during the main sequence due to larger convective cores.
- **Delayed hydrogen exhaustion**, allowing more gradual post-main-sequence expansion.
- **More luminous post-main-sequence evolution**, as the larger He cores retain more thermal energy.

Effects on Central Temperature-Density (T_c - ρ_c): A larger convective core due to CBM means that hydrogen burning proceeds at lower central densities and temperatures during the main sequence compared to models with less mixing. This results in:

- **Lower peak T_c during the main sequence**, reducing the rate of CNO cycle burning and leading to a longer-lived core.
- **A more massive helium core at H exhaustion**, which affects later burning stages.

6.3.2 CBM and Helium Burning: Effects on Core Structure and Mixing

During helium burning, CBM influences the extent of convective helium-burning cores, altering the He-burning lifetime and the eventual C/O composition of the core.

Trends in the HR Diagram:

- Models with **strong CBM** tend to have more extended blue loops during helium burning, as the additional mixing enhances the efficiency of core burning.
- Models with **less CBM** tend to transition into red supergiant (RSG) structures earlier, with less luminous blue loops.

Trends in T_c - ρ_c : More extensive CBM leads to:

- Lower central densities at He exhaustion, making the core less degenerate.
- Higher final He-core masses, influencing the onset of carbon burning.
- More gradual temperature evolution, delaying C ignition slightly in models with extended CBM.

6.3.3 CBM and Advanced Burning: Implications for Carbon and Oxygen Burning

CBM affects not only the convective boundaries of early burning stages but also the size and structure of the carbon-oxygen core at later stages, influencing the conditions for carbon ignition.

Effects on Carbon Burning: Models with stronger CBM tend to:

- Ignite carbon burning at slightly lower central densities due to their more massive C/O cores.
- Exhibit longer carbon-burning lifetimes, as mixing prolongs the availability of fuel.
- Form larger oxygen-rich cores, influencing later oxygen and silicon burning stages.

Effects on Oxygen Burning: The effects of CBM on O burning are primarily seen in:

- Onset of convective O burning—more extended CBM leads to stronger convective O-burning shells.
- Core-collapse characteristics—CBM influences whether the final remnant is a neutron star (NS) or a black hole (BH).

6.3.4 Implications for Supernova Progenitors and Final Remnants

The impact of CBM on the final fate of a massive star is significant:

- More CBM → Larger CO core: Increases the likelihood of forming a direct-collapse black hole.
- Less CBM → Smaller CO core: More favorable conditions for neutron star formation.
- Delayed ignition times: Leads to different pre-supernova structures, affecting supernova explosions and fallback accretion.

7 Pre-Supernova Abundance Analysis of Fundamental Elements

7.1 General Trends in ^{12}C

Across all masses, the cumulative ^{12}C yield does not vary monotonically with metallicity. Instead, for a given CBM efficiency the yield tends to peak at an intermediate metallicity and decline at both higher and lower Z . In our models:

- At solar metallicity ($Z = Z_{\odot}$), the high initial CNO content leads to rapid hydrogen burning, which limits the extent of helium burning and results in somewhat lower ^{12}C yields.
- Intermediate metallicities (e.g., around $Z = 10^{-4}$ or 10^{-5}) often optimize carbon production by striking a balance between sufficient seed nuclei and favorable core conditions.
- Zero-metallicity models ($Z = 0$) show intermediate yields, as carbon is produced primarily through the triple-alpha process in the absence of pre-existing heavy elements.

Notably, when comparing across masses, the $25 M_{\odot}$ models generally produce higher total ^{12}C yields than the 15 or $20 M_{\odot}$ models, reflecting the more energetic core conditions in higher mass stars. However, the relative influence of metallicity and CBM remains qualitatively similar.

7.1.1 Impact of Convective Boundary Mixing (CBM)

Enhanced CBM increases the overall ^{12}C yield by promoting more extensive mixing of helium into the core, which prolongs helium burning and facilitates carbon synthesis. For all three mass groups:

- Models with higher CBM rates (e.g., 5%) consistently yield higher cumulative carbon masses and exhibit smoother, more extended ^{12}C profiles.
- In contrast, models with lower CBM efficiencies (e.g., 0.5%) show yields that are more centrally concentrated, with steep gradients at the convective boundaries.

This effect is particularly significant at lower metallicities, where enhanced mixing can partially compensate for the lower initial carbon content by transporting the limited ^{12}C outward more efficiently.

7.1.2 Radial Distribution of ^{12}C Mass Fraction

The ^{12}C mass fraction profiles provide insight into the internal distribution of carbon at core collapse:

- In all models, X_{12C} is highest in the helium-burning core and declines sharply at the boundary between convective and radiative regions.
- With stronger CBM, the X_{12C} profile becomes smoother, and carbon is mixed into the outer layers, resulting in higher surface mass fractions.
- Although lower metallicity models naturally produce less carbon, high CBM rates can enhance the ^{12}C mass fraction in the envelope, illustrating an important interplay between mixing and initial composition.

7.1.3 Comparative Plots of M_{12C} vs. $\log(Z)$

- **Non-monotonic Dependence on Z :** Across all masses, M_{12C} does not consistently increase or decrease with metallicity; instead, many models display a peak yield at an intermediate Z (e.g., 10^{-4} or 10^{-5}), with lower yields at both higher (Z_{\odot}) and lower (10^{-7} , $Z = 0$) metallicities.
- **Impact of CBM Rate:** In general, higher CBM rates produce greater carbon yields. The 5% CBM lines (black) sit above the 2% (red) and 0.5% (blue) curves in most cases, reflecting how enhanced mixing extends the helium-burning core and transports newly synthesized carbon outward more efficiently.

- **Mass-Dependent Trends:** Comparing the three panels reveals that the $25 M_{\odot}$ models often achieve significantly higher M_{12C} than their 15 or $20 M_{\odot}$ counterparts at the same metallicity and CBM rate. This behavior highlights the more energetic core conditions in higher-mass stars, which favor stronger carbon production.
- **Zero-Metallicity and Very Low Z :** Even at $Z = 0$, the final carbon yield can be substantial, especially when CBM rates are high (2% or 5%). This result underscores the role of primary nucleosynthesis (triple-alpha) in generating carbon in primordial or extremely metal-poor environments, provided that mixing is sufficiently effective.

Overall, these comparative plots emphasize the intertwined effects of metallicity, mass, and mixing efficiency on carbon synthesis. While intermediate metallicities often yield the most carbon, stronger CBM can compensate for very low Z , and higher-mass stars are more sensitive to changes in both composition and mixing. The net result is a highly non-linear relationship between $\log(Z)$ and M_{12C} , reflecting the complexity of late-stage stellar evolution in massive stars.

7.1.4 Summary of Key Observations

- **Metallicity Dependence:** For each mass, carbon yields peak at intermediate metallicities and decline at both very high and very low Z . The absolute yields are higher in more massive stars.
- **CBM Effects:** Increased convective boundary mixing boosts both the total carbon yield and its outward transport, with the effect being most pronounced at low metallicities.
- **Mass Influence:** While the qualitative trends with metallicity and CBM are similar across 15 , 20 , and $25 M_{\odot}$ models, the higher mass models (especially $25 M_{\odot}$) exhibit a greater sensitivity to mixing, leading to significantly higher cumulative yields.
- **Combined Impact:** The final ^{12}C distribution in pre-supernova models is determined by a complex interplay among initial mass, metallicity, and convective boundary mixing efficiency, all of which have important implications for the chemical enrichment of the interstellar medium.

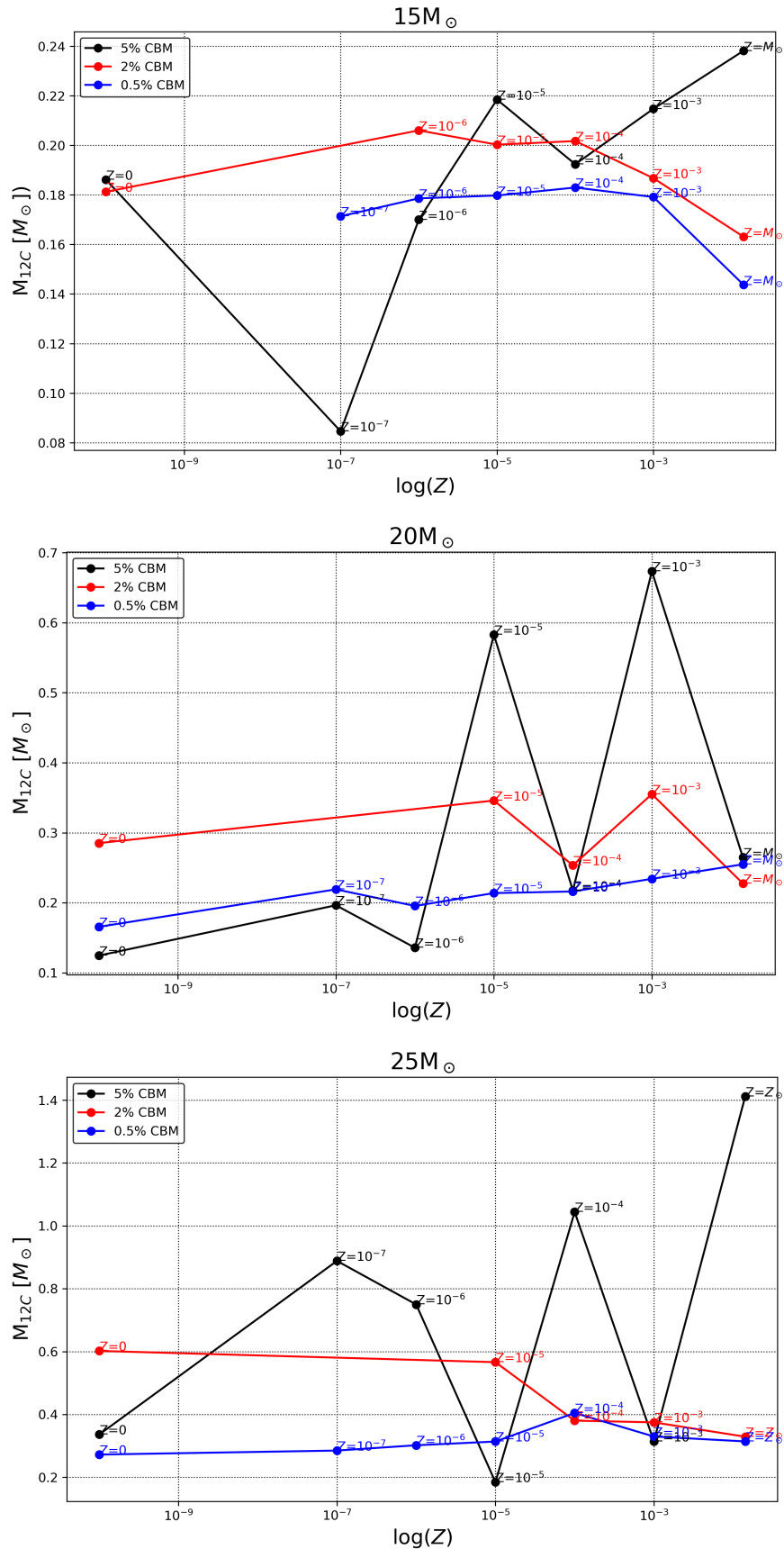


Figure 24: ^{12}C Mass Yield Comparisons for 15 , 20 and $25M_\odot$ star respectively.

7.2 General Trends in ^{14}N Yields

7.2.1 Metallicity Dependence

- **High Z (e.g., $Z_\odot, 10^{-3}$):** The presence of abundant CNO nuclei significantly enhances nitrogen production via the CNO cycle, often leading to higher M_{14N} . In all three mass ranges ($15, 20, 25 M_\odot$), solar and near-solar metallicities consistently yield the largest amounts of ^{14}N .
- **Low/Zero Z (e.g., $10^{-7}, 0$):** Here, ^{14}N synthesis relies on primary nucleosynthesis—initially forming carbon and oxygen through triple-alpha and subsequent α -capture before nitrogen can be produced. As a result, metal-poor stars yield less ^{14}N overall, though non-negligible amounts can still form if conditions allow.

7.2.2 Effect of Stellar Mass:

- **$15 M_\odot$:** Nitrogen yields tend to track metallicity closely, with a moderate but noticeable boost from increased CBM. These stars produce sufficient CNO elements for an active cycle, yet their smaller cores limit the total M_{14N} relative to more massive models.
- **$20 M_\odot$:** Slightly higher core temperatures and densities lead to greater overall ^{14}N production than in $15 M_\odot$ stars under comparable conditions. The interplay of metallicity and CBM can create more pronounced differences in final yields.
- **$25 M_\odot$:** The most massive models show the greatest sensitivity to mixing and metallicity, often exhibiting the widest range of M_{14N} values. Strong CBM and intermediate/high Z can lead to substantially elevated nitrogen yields, reflecting the vigorous nuclear burning in these stars.

7.2.3 Influence of CBM Rates:

- **Low CBM (0.5%):** Nitrogen-rich layers remain closer to the core, resulting in a more localized production zone. Yields are lower overall, particularly in metal-poor models.
- **Intermediate CBM (2%):** Enhanced mixing broadens the helium-burning region and redistributes CNO nuclei, increasing M_{14N} for most metallicities. The effect is more apparent in higher-mass stars, which have larger convective cores.
- **High CBM (5%):** The most substantial nitrogen production occurs with 5% CBM, especially at intermediate to high metallicities. Even low- Z models see a boost in M_{14N} due to the more efficient transport of newly formed carbon and oxygen, which subsequently feeds the CNO cycle.

7.2.4 Radial Distribution of ^{14}N Mass Fraction

1. **Core vs. Envelope:** In all masses and metallicities, X_{14N} peaks in or near the helium-burning core, where the CNO cycle is most active. Without strong mixing, nitrogen remains confined to this region. As CBM rates increase, nitrogen is carried into outer layers, creating smoother abundance gradients.

2. Metallicity Influence:

- **High Z :** Significant ^{14}N enrichment occurs throughout the core and into the envelope, especially with 5% CBM, leading to relatively flat abundance profiles at larger radii.
- **Low Z :** At very low or zero metallicity, the star must first synthesize carbon and oxygen before nitrogen can form. Higher CBM partially compensates by mixing these elements outward, but overall $X_{14\text{N}}$ remains modest relative to high- Z stars.

3. Mass Effects on Distribution: Larger cores in 20 and 25 M_\odot stars facilitate more extended burning zones, thus producing and distributing ^{14}N over a broader radial range. In contrast, 15 M_\odot models often show steeper gradients unless mixing is particularly strong (5% CBM).

7.2.5 Summary of Key Observations

- **Peak Yields at High/Intermediate Z :** Regardless of mass, stars with solar or near-solar metallicities produce the most ^{14}N , benefiting from an ample initial CNO reservoir. Intermediate metallicities can also yield robust nitrogen if the star's core conditions and mixing rates are favorable.
- **Sensitivity to CBM:** Stronger convective boundary mixing (2–5%) consistently raises $M_{14\text{N}}$ across all masses and metallicities, smoothing radial abundance profiles and boosting outer-layer nitrogen content.
- **Mass Dependence:** While the overall trends hold for 15, 20, and 25 M_\odot stars, higher-mass models (especially 25 M_\odot) display the largest absolute yields and the greatest range of ^{14}N production, reflecting their more energetic core environments.
- **Low Z Production:** Although ^{14}N yields are naturally lower at $Z \approx 0$, strong mixing can partially offset the lack of seed nuclei, enabling metal-poor stars to synthesize measurable amounts of nitrogen.

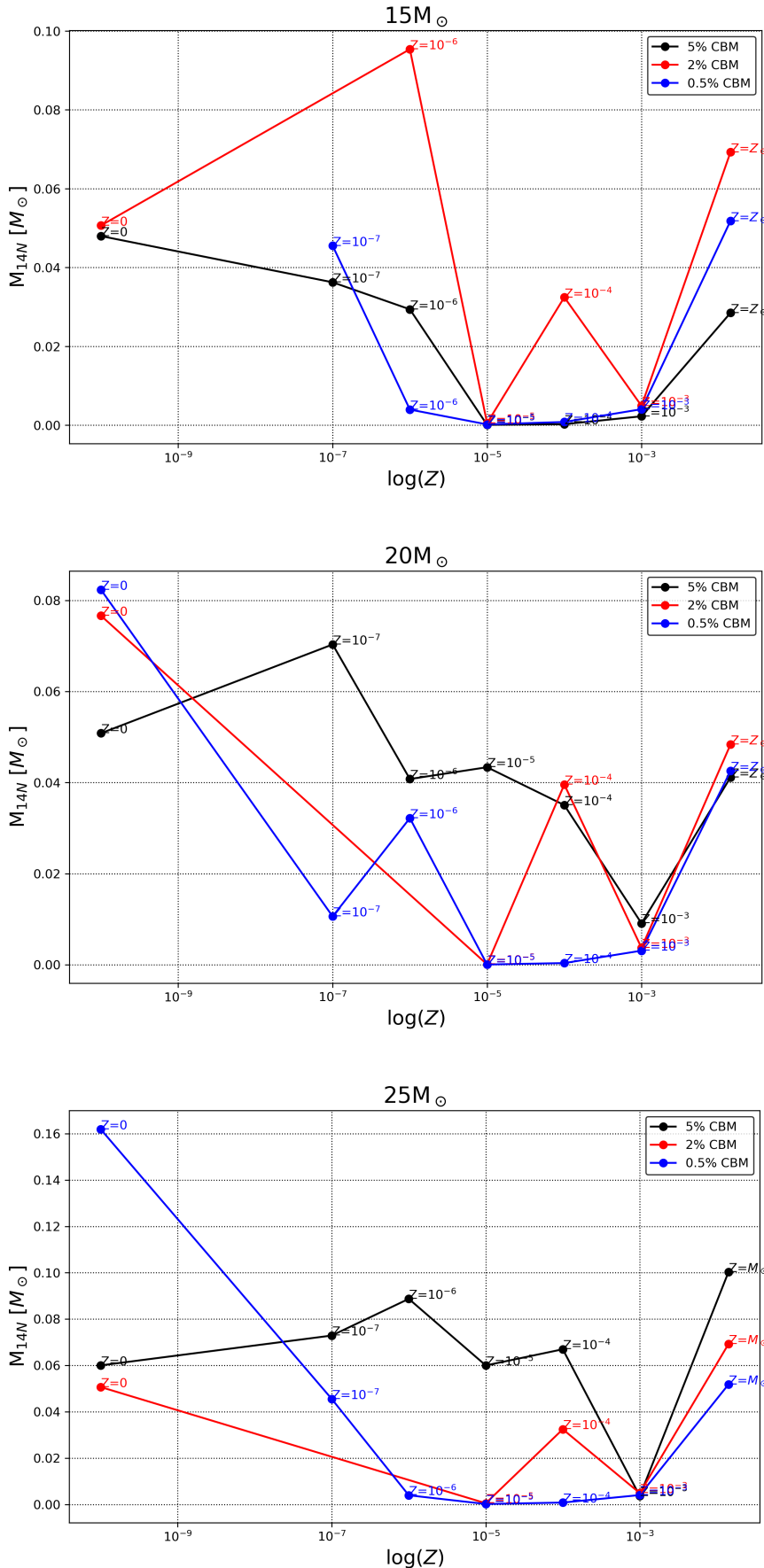


Figure 25: ^{14}N Mass Yield Comparisons for 15 , 20 and $25M_\odot$ star respectively.

7.3 General Trends in ^{16}O Yields

7.3.1 Metallicity Dependence

- **High Z (e.g., $Z_\odot, 10^{-3}$):** Ample initial CNO elements drive robust helium burning and α -capture, leading to elevated $M_{16\text{O}}$. Across all three masses ($15, 20, 25 M_\odot$), near-solar metallicity models tend to produce the most oxygen, thanks to efficient nuclear processing of pre-existing metals.
- **Intermediate Z (e.g., $10^{-4}, 10^{-5}$):** Some models show a peak in ^{16}O yield at intermediate metallicities, reflecting an optimal balance between core burning conditions and available seed nuclei. This trend is slightly more pronounced in higher-mass stars, which can capitalize on stronger core temperatures and densities.
- **Low/Zero Z (e.g., $10^{-7}, 0$):** Here, ^{16}O forms primarily via triple-alpha reactions followed by α -capture on ^{12}C . While total yields can still be substantial, they typically lag behind high- Z cases unless the CBM rate is sufficiently large to expand the helium-burning region.

7.3.2 Impact of Stellar Mass

- **$15 M_\odot$:** Oxygen yields reflect a moderate interplay between metallicity and CBM. The smaller convective core relative to higher-mass stars restricts the region where α -capture can occur, although strong mixing (5% CBM) can still boost $M_{16\text{O}}$ significantly.
- **$20 M_\odot$:** Higher core temperatures and densities lead to generally larger ^{16}O yields compared to $15 M_\odot$, but the same metallicity and CBM trends hold. Intermediate metallicities or near-solar Z combined with robust mixing often produce the highest oxygen yields.
- **$25 M_\odot$:** These stars show the greatest sensitivity to both composition and CBM. Their larger cores and more vigorous burning can amplify differences in Z and mixing efficiency, resulting in the widest range of possible oxygen yields.

7.3.3 Effect of CBM Rates

- **Low CBM (0.5%):** Oxygen production is more localized in the core, yielding steep abundance gradients. In low-metallicity stars, $M_{16\text{O}}$ remains relatively modest, as the smaller active burning zone limits primary nucleosynthesis.
- **Intermediate CBM (2%):** Enhanced mixing broadens the helium-burning region, increasing $M_{16\text{O}}$ across all metallicities. The effect is evident for each mass, but more so in 20 and $25 M_\odot$ models with larger cores.
- **High CBM (5%):** Strong overshoot mixing maximizes oxygen yields by extending and prolonging helium burning. Even at $Z = 0$, 5% CBM can compensate for a lack of seed nuclei, raising $M_{16\text{O}}$ well above what would be possible under weaker mixing.

7.3.4 Radial Distribution of ^{16}O Mass Fraction

1. Core vs. Envelope: In all masses and metallicities, $X_{16\text{O}}$ typically peaks near the helium-burning core. Without robust mixing, oxygen remains confined to deeper layers, resulting in sharp boundaries at the convective/radiative interface. As CBM rates increase, oxygen is transported into more external zones, smoothing the abundance gradient and enhancing surface enrichment.

2. Metallicity and Mixing Interaction

- **High Z :** Strong pre-existing CNO content drives efficient α -capture, and high CBM spreads ^{16}O outward, creating relatively uniform profiles in the outer envelope.
- **Low/Zero Z :** Oxygen must be built up from primary processes. While yields are lower, strong CBM (5%) partially offsets the limited initial metals by expanding the effective burning region and redistributing newly formed ^{16}O into the envelope.

7.3.5 Summary of Key Observations

- **Metallicity Dependence:** Near-solar or intermediate Z typically maximize oxygen yields, though extremely metal-poor stars can still produce notable ^{16}O if mixing is sufficiently high.
- **Mass Effects:** Higher-mass stars (20 and $25 M_\odot$) exhibit greater sensitivity to both metallicity and CBM, often achieving larger absolute yields and broader enrichment regions than $15 M_\odot$ models.
- **Role of CBM:** Increasing CBM from 0.5% to 5% consistently boosts $M_{16\text{O}}$ and spreads oxygen into the outer layers. This effect is particularly crucial at low Z , where it compensates for the lack of initial seed nuclei.
- **Radial Profiles:** Minimal mixing confines ^{16}O to the core, resulting in steep $X_{16\text{O}}$ gradients, while robust mixing yields smoother distributions and extends oxygen enrichment outward.

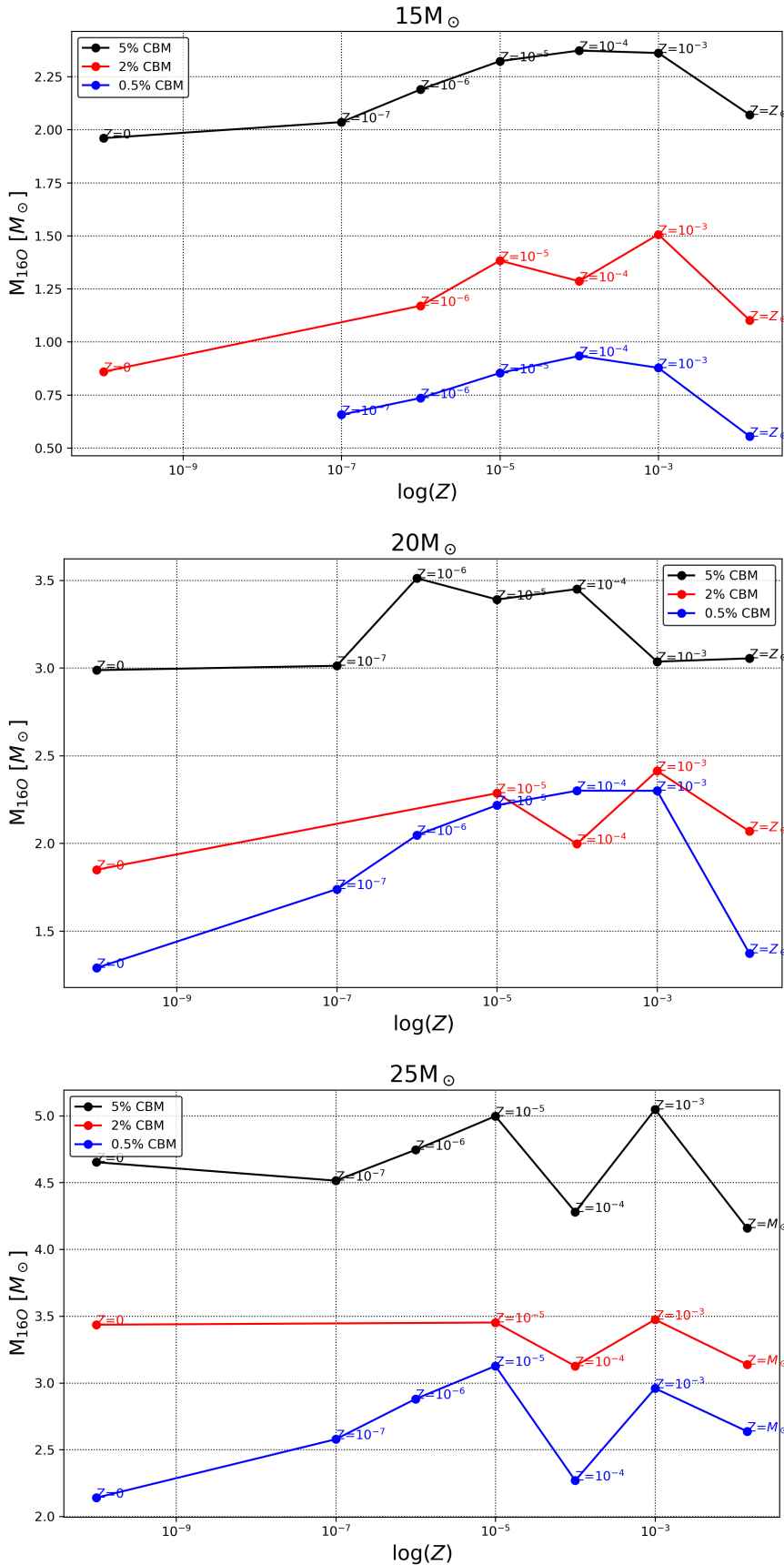


Figure 26: ^{16}O Mass Yield Comparisons for 15 , 20 and $25M_\odot$ star respectively yr.

8 Conclusion

This study has demonstrated that the evolution and final nucleosynthetic yields of massive stars depend on a delicate interplay among stellar mass, initial metallicity, convective boundary mixing (CBM), and nuclear network selection. Higher masses produce hotter, denser cores that favor more vigorous burning, while richer metallicities provide a larger initial reservoir of CNO elements that drive efficient synthesis of ^{12}C , ^{14}N , and ^{16}O . Enhanced CBM extends convective regions, increases core growth, and redistributes nuclear ashes outward, thereby boosting elemental yields even in metal-poor stars via primary nucleosynthesis.

In summary:

- **Mass and Metallicity:** Higher-mass stars (e.g., $25 M_{\odot}$) generally yield more elements than lower-mass stars, while intermediate to high metallicities optimize the production of ^{12}C , ^{14}N , and ^{16}O .
- **Convective Mixing:** More efficient CBM (e.g., 5%) expands the burning regions and smooths out the internal distribution of elements, compensating for low initial metallicity by enhancing primary nucleosynthesis.
- **Nuclear Networks:** The choice of nuclear reaction network affects core composition and burning conditions, with more extensive networks promoting stronger mixing and earlier ignition stages.

Overall, the final nucleosynthetic output is governed by a complex balance of these factors, which in turn influences the type of compact remnant formed and the star's role in galactic chemical enrichment. Understanding these interdependencies is essential for predicting the initial mass function (IMF) of remnants and the chemical evolution of galaxies.

9 References

1. Clayton, D. D. (1968). *Principles of Stellar Evolution and Nucleosynthesis*. University of Chicago Press.
2. Arnett, W. D. (1996). *Supernovae and Nucleosynthesis: An Investigation of the History of Matter, from the Big Bang to the Present*. Princeton University Press.
3. Hix, W.R. and Thielemann, F.-K., (1996), *Silicon Burning. I. Neutronization and the Physics of Quasi-Equilibrium*. *Astrophys. J.*, 460, 869.
4. Kippenhahn, R., Weigert, A., & Weiss, A. (2012). *Stellar Structure and Evolution*. Springer.
5. Woosley, S. E., & Janka, T. (2005). "The Physics of Core-Collapse Supernovae." *Nature Physics*, 1(3), 147-154.
6. Paxton, B., Bildsten, L., Dotter, A., Herwig, F., Lesaffre, P., & Timmes, F. (2011). "Modules for Experiments in Stellar Astrophysics (MESA)." *The Astrophysical Journal Supplement Series*, 192(1), 3.